THE UNIVERSITY OF MELBOURNE

School of Physics

Defect Study of Phosphorus Implanted Silicon for Quantum Computing

Matthew Lay

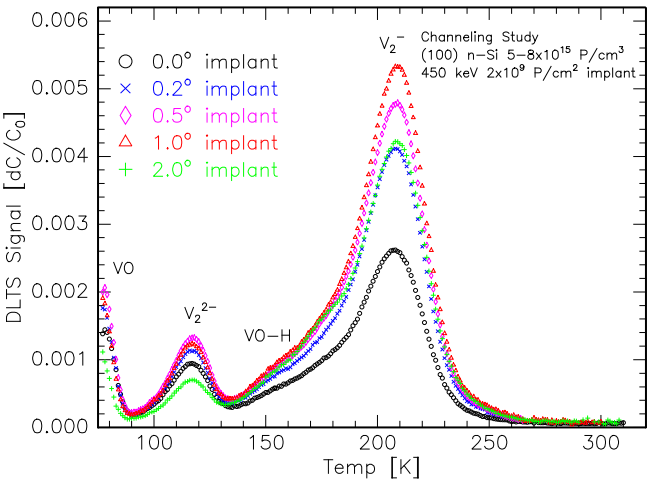

Honours Report (Revised), 2001

Supervisor: Dr. Jeff C. McCallum

Abstract

The defects introduced in P implanted n-type silicon have been studied as a function of implantation angle and subsequent annealing temperature for 75 keV and 450 keV P ion implantations. Samples were Rapid Thermal Annealed for 15 minutes at temperatures up to 400^{o}C. Analysis involved electrical techniques, Deep Level Transient Spectroscopy (DLTS) and Capacitance-Voltage (C-V) measurements, as well as Ion Beam techniques, Channeling Rutherford Back–Scattering (RBS-C). From these techniques it was possible to determine the: bulk defect concentrations, defect concentration depth profiles, and the defect species present as characterised by their different energy band levels and capture cross-sections as a function of implant angle.

Thank you.....

To my parents for allowing me this opportunity to learn that dreams are realisable
and that goals are attainable.

David Hoxley, Sean Hearne and Brett Johnson. Thank you for letting my ego into room 210 and helping me through the year. Thanks in particular to Brett for being such a cool person with a seemingly unlimited supply of energy and genplot commands, and David for being like my big brother.

To the entire MARC for making my experience this year an enjoyable one.
Thanks also Amelia Liu for being like my big sister.

Yvan Dang, for reminding me that it's important to live a balanced life and for your attempts to keep me sane in an otherwise insane world.

To the Special Research Center for Quantum Computer Technology for the financial support for all my trips to Canberra.

Dr. P. N. K 'Sanju' Deenapanray and Prof. C. Jagadish. I am indebted to you for teaching me the art of defect studies and DLTS as well as for the use of your equipment at the ANU. Thank you also to Dr. Gustavo Azevedo for performing all the MARLOWE simulations despite your busy schedule.

Lastly, thank you Jeff, for living up to the reputation for being the best supervisor around, and for answering all of my 'quick questions' through the year. Your patience and understanding made this project possible.

List of Figures

List of Tables

Contents

Chapter 1

Introduction

1.1 Kane Architecture for a Quantum Computer

A scalable quantum computer may be realised with the solid state Kane architecture [3]. This design consists of a spin-0 ^{28}Si lattice embedded with an array of spin-$\frac{1}{2}$ ^{31}P nuclei as qubits for computation. The P nuclear spins are to be controlled using nuclear magnetic resonance (NMR), and in order to separately address each nuclear spin their NMR frequency is to be varied by adjusting the hyperfine interaction between the P nuclei and their valence electron. Quantum computation also requires entanglement of nuclei which is to be achieved via electron mediated spin coupling between P nuclei. Control is to be achieved by interacting with the electrons via an applied electric field from gates on the surface which will draw the P valence electrons closer to the surface of the device.

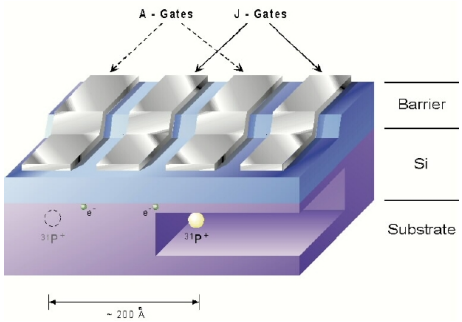

Figure 1.1: Solid state Kane quantum computer design.

1.2 Top Down Fabrication and Defect Study

As a first step, the Special Research Centre for Quantum Computer Technology aims to fabricate such a quantum computer using ion implantation to create the ordered array of P nuclei in silicon. Native point defects exist in all silicon wafers however and implantation of phosphorus into silicon will create additional defects. Some of these defects will be electrically active and trap electrons in the semiconductor, this poses a problem for the operation of the quantum computer due to its electron based control. Defect generation therefore needs to be well understood in order to minimise it.

It will also be necessary to implant P ions through a mask to fabricate the array. The high aspect ratio of the mask required will result in the ions being implanted into silicon with a small implantation angle with respect to the surface normal of the wafer. These small implantation angles will result in the ions being channeled into the silicon lattice which will affect the distribution and concentration of defects introduced. This aspect of channeled ions has not been extensively explored in the past due to the semiconductor industry's deliberate avoidance of channeled implantation [4].

Defects can be removed to some extent by thermal annealing of the device after implantation and the effectiveness of this also needs to be explored in detail.

Although it is possible to analyse the defects introduced into ion implanted silicon in a similar low dose regime to what will be required for the fabrication of the Kane quantum computer, there is no direct method of analysing the defects introduced in the energy regime that will be required. It will therefore be necessary to utilise some sort of model to predict the distribution and concentration of defects. This project has set out to provide fundamental data in order to test these models in regimes where the defects produced can be analysed with existing analytical techniques. In particular the critical region between the surface and the implanted P qubits needs to be examined.

Such a comprehensive defect study of implanted P in Si has not previously been conducted, especially with regard to channeling implantation. Results from this project will aid in determining the optimal parameters for fabricating the quantum computer with minimal defects, as well as providing useful data for the semiconductor industry as it moves towards creating devices in regimes that will involve a greater fraction of channeled ions.

Chapter 2

Background

2.1 Channeled Ion Implantation

Ion implantation is usually performed in the interest of modifying the electrical characteristics of the substrate material being implanted. The implanted ions interact with atoms in the substrate in a stochastic manner and the final resting place for the ions can only be specified with some probability. The implantation involved in the fabrication of electronic devices in the semiconductor industry also requires strict control on the depth of the implanted ions due to their planar design. This can be achieved if the ions are implanted into the substrate in such a direction that the ion *sees* an essentially random distribution of atoms (fig. 2.1a). This results in the ions being quickly stopped and the depth profile of implanted ion concentration having a well defined distribution (see fig. 2.2).

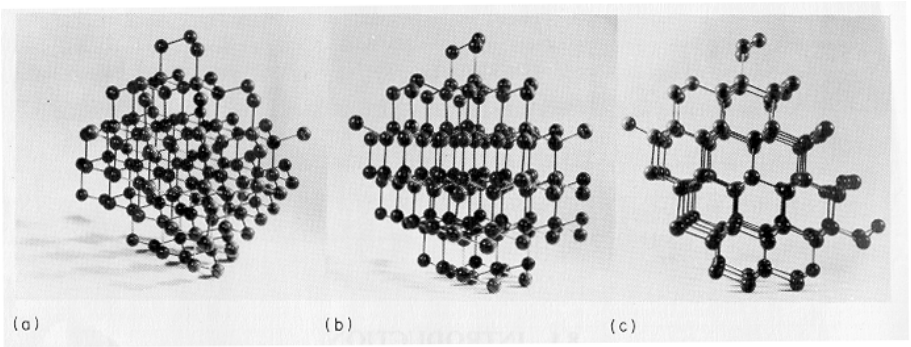

Figure 2.1: The lattice of crystalline silicon viewed in various orientations (a) Random, (b) planar channeling, (c) axial channeling [1].

Due to the crystalline lattice structure of silicon the lattice planes or axial rows of atoms in it (fig. 2.1b,c) can guide or channel the ions in certain directions with a series of small angle collisions [1] which result in a broadened depth profile. The increase in spread or straggle in depth however is at the expense of the lateral straggle which is smaller in comparison. This decrease in lateral straggle is beneficial since it improves alignment of the gates with the underlying P array for the fabrication requirements of the Kane quantum computer.

2.2 Point Defects

It has been well established that ion implantation introduces many defects into the substrate [5, 6, 7]. In particular Frenkel defects are created which consist of a host atom that has been knocked off its substitutional lattice site into an interstitial position (i.e. between crystal lattice sites) leaving a vacancy behind in the lattice [7]. At room temperature the vacancy and interstitial can migrate and separate without recombination. This occurs for 4-10% of the Frenkel defects created during ion implantation [7]. These defects can go on to cluster

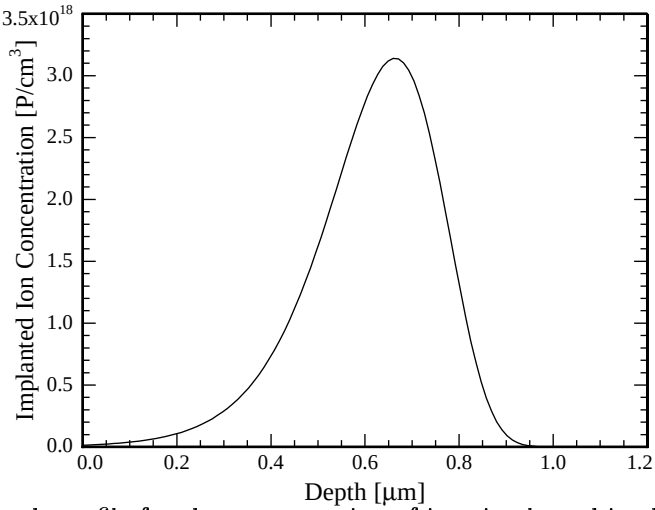

Figure 2.2: A typical depth profile for the concentration of ions implanted in the random orientation as used by the semiconductor industry.

together or form stable defect complexes with impurities. About 10-25% of the Frenkel defects that survive recombination form a di-vacancy cluster [8] which is a characteristic defect for ion implanted silicon [5, 9].

The defects of prime importance for electrical devices are those that are electrically active, meaning that they can trap charge carriers in the device. Electrically active traps are basically unoccupied states in the band-gap of a semiconductor that trap charge carriers. This occurs mostly due to defects having dangling bonds which are unpaired electrons, and the traps exist at some energy level depending on the structure of the defect. Identification of defect structures and atomic constituents is achieved most reliably with Electron Para-magnetic Resonance (EPR) measurements although not every defect complex has an EPR signature. The identity of defects which do not show up in EPR are often inferred from detailed analysis of their annealing characteristics.

In the case of ion-implanted phosphorus doped silicon the interstitial silicon does not form a trap, but the vacancies can migrate and combine with impurities such as oxygen and carbon (found in even top grade commercially available silicon wafers) as well as with the phosphorus dopant to form vacancy complexes. Chemical cleaning of the silicon can also lead to incorporation of hydrogen which is believed to be the constituent of many defect complexes.

Defects can be characterised by their position in the band-gap of a semiconductor relative to the conduction band (trap energy, E_t), and their cross-section for trapping (capture cross-section, σ). The values reported for electron traps in ion-implanted silicon are found in table 2.1. This table shows the average value for the trap energies found in the literature. Absolute errors in the last digit are shown in parentheses, no error is quoted for occasions where there is only one reference for the defect, nor is the error quoted for capture cross-sections that have an error that is over an order of magnitude difference. V indicates vacancy, other letters indicate elements, subscripts 2 & 3 indicate the number of vacancies in a cluster and superscripts indicate the charge state of the trap. Other subscripts indicate either substitutional or interstitial atomic positions in the lattice.

Although high dose channeled implanted Si has been previously analysed for extended defects with techniques such as Cross-sectional Transmission Electron Microscopy (XTEM) and Channeling Rutherford Backscattering (RBS-C) [10, 11, 12], there has only been one paper found regarding low dose channeled implanted Si and the generation of point defects [4]. However, this last paper deals with He ion irradiation which is expected to create a different range of defects from the implantation of heavier P ions.

2.3 Thermal Annealing

The created defects in as-implanted materials may be removed by annealing at some sufficiently high temperature. Device annealing is usually performed as Rapid Thermal Annealing (RTA) which involves use of a IR lamp array to rapidly heat the device up to a desired temperature and then maintain it for a suitable time, usually up to 30 minutes at most.

Different defects however have different thermal stabilities and the dissociation of one species of defects can result in the creation of others from the by-products. The annealing behavior of defects has been studied over the

years by many people by examining how the defects concentration changes upon annealing. The characteristics for defects relevant to ion implanted n–type silicon are shown in table 2.2. The reverse annealing temperature indicates that the defect is observed to increase in concentration after an anneal at this temperature or that it is first observed at this temperature. The annealing temperature indicates the temperature required to reduce the defect below the detection limit.

Defect type	Trap Energy [ev]	Capture cross–section [cm^2]	References
H–related	0.10	–	[13]
H–related	0.13	–	[13]
HC	0.15(1)	–	[14, 15]
VO	0.17(1)	$7(4)x10^{-15}$	[15, 16, 17, 18, 19, 20, 21, 22, 23, 24]
C_sC_i	0.17(0)	$8x10^{-18}$	[7, 23]
V–related	0.19(1)	$3.5x10^{-17}$	[16, 24]
V_2^{2-}	0.22(1)	$5(4)x10^{-16}$	[7, 15, 16, 17, 18, 19, 20, 21, 22, 24]
V_2O	0.27	–	[7]
V_3O	0.30	–	[7]
VO-H, other H–related	0.30(2)	$3x10^{-15}$	[13, 15, 22, 17, 24, 25]
V–related	0.35(1)	$5x10^{-16}$	[17, 18]
H–related	0.39(1)	$1x10^{-17}$	[16, 17]
H–related	0.41(1)	–	[13, 19]
VP_s	0.42(2)	–	[7, 13, 16]
V_2^-	0.42(1)	–	[7, 15, 16, 18, 20, 21, 22, 24]
H–related	0.45(1)	$1x10^{-17}$	[13, 16, 24, 25]
V_2–related	0.47	–	[16]
H–related	0.50(1)	–	[15, 22]
Unknown	0.59	–	[24]

Table 2.1: Defect characteristics as published in the literature for defects relevant to ion-implanted n-type silicon.

Defect type	Reverse Annealing Temperature [^oC]	Annealing Temperature [^oC]	References
VO	–	370	[7, 21, 24]
C_sC_i	–	220	[7]
V–related (0.19 eV)	300	300+	[24]
$V_2^{2-/-}$	–	300	[21, 24, 7]
V_2O	–	300	[7]
V_3O	–	450	[7]
VO-H	200	300+	[21, 24]
VP_s	–	150	[24, 7]
Unknown (0.59 eV)	300	300+	[24]

Table 2.2: Annealing characteristics as published in the literature for defects relevant to ion-implanted n-type silicon.

2.4 Electrical Analysis of Semiconductors

Deep level transient spectroscopy (DLTS) was the principle technique used in this project to evaluate defect concentration levels as well their trap energy and capture cross-section. By comparing these characteristics as well as the annealing behavior of the defects, to the characteristics and annealing behavior of the defects outlined in table 2.2 it is possible to identify the species of defects present in the samples.

DLTS uses the fact that the energy levels of the deep level traps are affected by the energy band bending at the interface between the semiconductor sample and a metal contact. This metal–semiconductor interface forms a Schottky barrier diode. By varying the extent of the band bending by applied biases traps can be filled

and emptied. This has an affect on the capacitance of the diode which can be measured and the signal analysed to evaluate the defect concentration and to characterise the defects present. To understand how this is possible it is necessary to first describe the Schottky diode.

2.4.1 Schottky Barrier Diodes

Schottky diodes can be fabricated on doped semiconductor surfaces to facilitate electrical characterisation of the sample. A Schottky diode is simply a metal–semiconductor interface that exhibits current rectifying properties across this interface similar to a p-n junction diode except that the Schottky diode characteristics only depend on the majority carrier electrons [26]. This discussion will focus on the characteristics of a n-type semiconductor Schottky diode.

The rectification is a result of the Schottky barrier formed at the interface due to the different work functions of the metal (ϕ_m) and semiconductor (ϕ_s). This barrier is characterised by a barrier height (ϕ_b), see fig. 2.3.

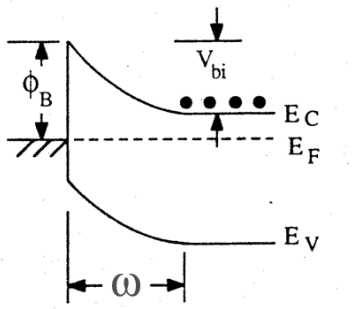

Figure 2.3: The bending of the energy bands for a n-type semiconductor Schottky barrier diode [2].

Due to the band bending there is a region in the semiconductor that has been emptied of charge carriers and has a net charge. This is the depletion region characterised by a width ω as seen in figure 2.3. The depletion region can be expressed as:

$$\omega = \sqrt{\frac{2\epsilon}{qn_D}(V_{bi} - (\frac{k_bT}{q}) - V)} \tag{2.1}$$

Where ϵ is the dielectric constant of the semiconductor, n_D the concentration of dopants in the semiconductor, V_{bi} the built–in voltage, and V the externally applied bias, as shown in figure 2.3.

The capacitance of the Schottky diode can be determined by considering the depletion region as a dielectric of width (ω) separating the metal contact of area (A) parallel to the edge of the depletion region in the semiconductor:

$$C = \frac{\epsilon A}{\omega} \tag{2.2}$$

Substituting equation 2.1 into 2.2 we have:

$$C = A\sqrt{\frac{\epsilon q N_D}{2(V_{bi} - (\frac{k_bT}{q}) - V)}} \tag{2.3}$$

2.4.2 Deep Level Transient Spectroscopy (DLTS)

Figure 2.4 shows an applied voltage pulse cycle required for DLTS. The sample is initially at a zero or some small bias V_0 and the traps in region II and III are filled with electrons (fig. 2.5a). Figure 2.5b shows that upon reduction of the bias to some lower negative (reverse) bias, the traps in region II begin to empty as the band bending makes it energetically favourable for the electrons to spill over into the conduction band of the semiconductor.

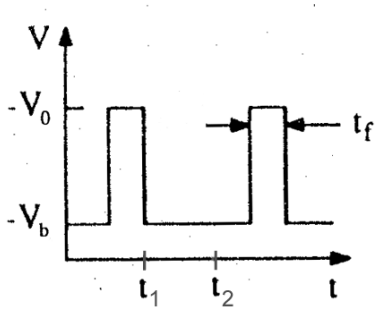

Figure 2.4: Required pulse cycle for DLTS [2].

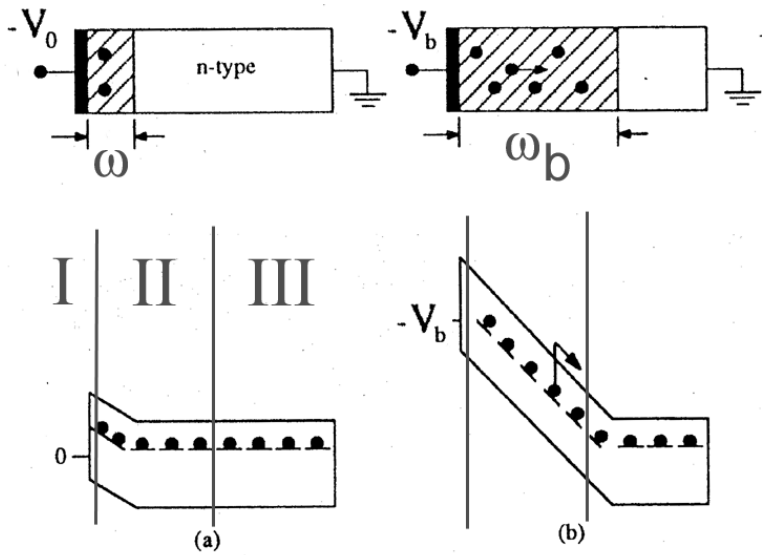

Figure 2.5: Deep level traps fill and empty depending on the applied bias [2].

This emission is described by an exponential function that depends on the total concentration of filled traps in region II $[n_T(t_1)]$ and an emission rate $[e_n]$:

$$n_T(t) = n_T(t_1)e^{-e_n t_2} \tag{2.4}$$

The emission rate (e_n) depends on temperature (T), the trap energy level (E_T) and the capture cross section (σ_c) of the trap:

$$e_n = \gamma_n \ \sigma_c \ T^2 e^{-(\frac{E_c - E_T}{k_B \ T})} \tag{2.5}$$

γ_n is a set of constants given by:

$$\gamma_n = 2\sqrt{3}M_c(2\pi)^{\frac{3}{2}}k_b^2 m^* h^{-3}$$

Where M_c is the number of minima in the conduction band of the semiconductor and m^* is the effective electron mass in it [27]. Since the trap energy level and the capture cross section characterise different defects this emission rate may be different for each defect.

Figure 2.6 shows how the capacitance of the Schottky diode changes over time as a result of the traps emptying. This capacitance transient can be expressed as:

$$C = C_0\sqrt{1 - \frac{n_T(t)}{n_D}} \tag{2.6}$$

For the case where $n_T << n_D$ we have:

$$C \approx C_0(1 - \frac{n_T(t)}{2n_D}) \tag{2.7}$$

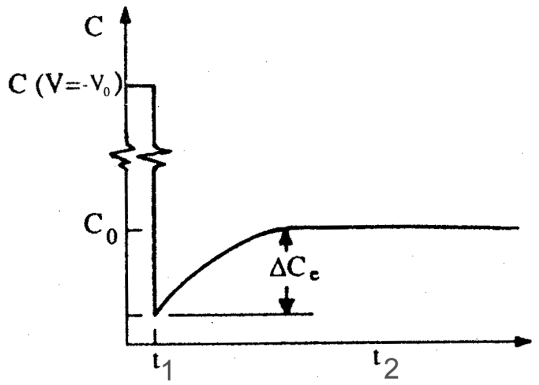

Figure 2.6: The time variation of capacitance as traps empty [2].

If we now monitor the change in capacitance over some time interval (measurement window) (t_1, t_2) the change in capacitance over the rate window [δ C] divided by the final capacitance [C_0] forms our DLTS signal (S) which can be written as:

$$S = .\frac{\delta\ C}{C_0} = [1 - \frac{\omega_0^2}{\omega_b^2}]\ \frac{n_t}{2n_d}\ [e^{-e_n(T)t_1} - e^{-e_n(T)t_2}] \tag{2.8}$$

Where ω_0 and ω_b are the depletion regions under zero and reverse bias respectively.

Figure 2.7 shows how the signal changes as a function of temperature when a single trap is present. This occurs due to the temperature dependence of the emission rate and it is a plot of the DLTS signal as a function of temperature that forms a DLTS spectrum. The bias voltage is again returned to the higher V_0 value for some filling pulse time [t_p] to fill the traps again and the cycle is repeated. This allows many readings to be taken to average the signal over.

Also, since the emission rate depends on the trap energy level of the defect responsible for the signal and its capture cross-section (eq. 2.5) each peak is characteristic of a defect in the sample.

Note that in equation 2.8, if the trap concentration n_T is zero then the signal is also zero. This is to say that the magnitude of the DLTS signal is also proportional to the concentration of defects present, n_T, and can be expressed as:

$$\left.\frac{\delta\ C}{C_0}\right|_{max} = \frac{n_T}{2n_D}\frac{1-r}{r^{\frac{r}{r-1}}} \tag{2.9}$$

Where r = $\frac{t_2}{t_1}$. We can then write for the trap concentration:

$$n_T = 2\left.\frac{\delta\ C}{C_0}\right|_{max} n_D \frac{r^{\frac{r}{r-1}}}{1-r} \tag{2.10}$$

Note that it is also important to know the concentration of electrically active dopants in the same region that is being probed to determine the defect concentration in that region. This is determined with separate C-V measurements to be discussed below.

By taking DLTS signals at various rate windows we may obtain a range of values for the peak temperature associated with each defect. Using these values and noting that at the peak temperature the emission rate is given by:

$$e_n(T_{peak}) = \frac{ln(\frac{t_2}{t_1})}{t_2 - t_1} \tag{2.11}$$

returning to equation 2.5 we may re–arrange it to give:

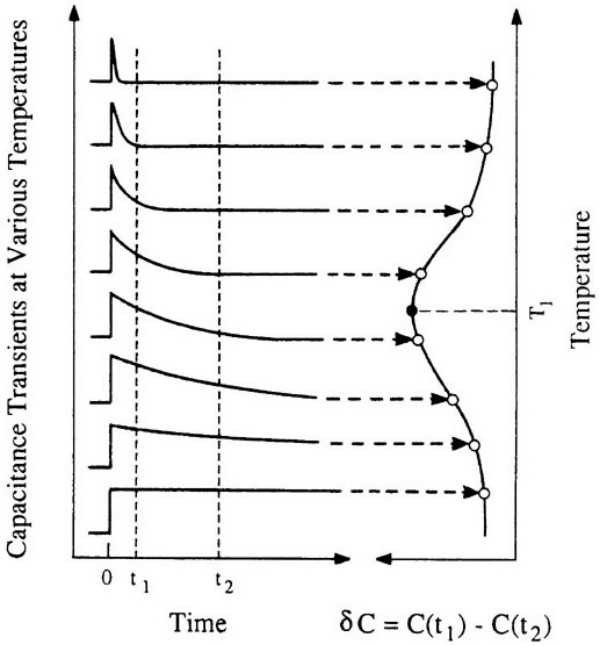

Figure 2.7: The temperature dependence of the DLTS signal [2].

$$e^{-(\frac{E_c - E_T}{k_B\ T})} = \frac{e_n}{\gamma_n\ \sigma_c\ T^2}$$

$$-(\frac{E_c - E_T}{k_B\ T}) = ln(\frac{e_n}{T^2} - ln(\gamma_n\ \sigma_c)$$

$$ln(\frac{e_n}{T^2}) = ln(\gamma_n\ \sigma_c) - (\frac{E_c - E_T}{k_B\ T}) \tag{2.12}$$

If we now take the temperature at each of the DLTS peaks and the associated emission rate as given by equation 2.11 we have a method of determining the trap energy level and capture cross section of the defect. This is achieved by producing an Arrhenius plot of $\ln(\frac{e_n}{T^2})$ vs. $\frac{1}{T}$. The trap energy level can then be found from the slope and the capture cross section from the intercept.

2.4.3 Capacitance–Voltage (C–V) Measurements

By varying the applied voltage while measuring the capacitance we can determine the concentration of electrically active dopants in the semiconductor and the built–in voltage of the diode (which will be important for discussion of the DLTS results later on). Rearrange equation 2.3:

$$\frac{1}{C^2} = \frac{2(V_{bi} - \frac{k_b\ T}{q} - V)}{\epsilon\ qA^2 n_D} \tag{2.13}$$

So if we plot $\frac{1}{C^2}$ against applied voltage V we may obtain the doping concentration from the slope $d(\frac{1}{C^2})dV$ and the built in voltage from the intercept V_{int}:

$$n_A(D) = -\frac{C^3}{q\epsilon\ A^2(\frac{dC}{dV})} = \frac{2}{q\epsilon A^2(\frac{d(\frac{1}{C^2})}{dV})} \tag{2.14}$$

$$V_{bi} = \frac{k_b T}{q} - V_{int} \tag{2.15}$$

2.4.4 DLTS Depth Profiling

It is possible to use DLTS to probe the defect concentration level of a specific defect and determine how it changes with depth, hence producing a depth profile for the defect. This is achieved by fixing the temperature of the sample at the temperature at which the defect produces a peak DLTS signal, placing the sample under reverse bias (as in DLTS), and then running a series of filling pulses that vary in amplitude by some small amount. By doing this we probe a different slice of the sample with each voltage pulse. These slices are shown as light gray sections in figure 2.8.

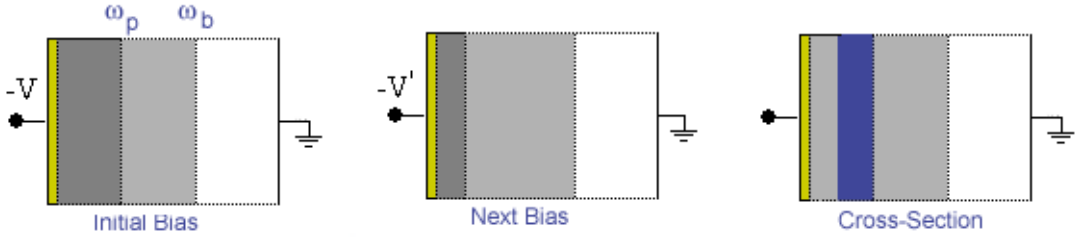

Figure 2.8: DLTS filling pulses allows determination of defect concentration in a cross–sectional slice of the sample.

The defect concentration in the blue cross-sectional slice shown in figure 2.8 can be determined by calculating the change in defect concentration between the initial slice (small voltage pulse) and the final larger slice (larger voltage pulse). This is essentially calculating the change in concentration with depth since the two slices correspond to two different depths.

Defect concentration is given by equation 2.10 which depends on the DLTS signal and depths depend on the reverse bias voltage and the filling pulse voltage as from equations 2.2 & 2.3. So, the change in defect concentration with depth can be expressed as the change in DLTS signal with voltage. This gives the following expression for the defect concentration in the small cross sectional slice:

$$n_t = \frac{q}{\epsilon_0 \epsilon_s} n_{D(\omega b)} n_{D(\omega_p)} \omega_b^2 \left(\frac{\omega_p}{\omega_p - \lambda}\right)\left(\frac{dS}{dV}\right) \tag{2.16}$$

Where ω_b is the width of the depletion region under reverse bias, ω_p is the depletion width under the pulse voltage, $n_{D(\omega)}$ is the doping concentration at depth ω, and $\frac{dS}{dV}$ is the change in DLTS signal with voltage. λ here is a correction factor for non-uniform doping and trap concentrations [28] and is given by:

$$\lambda = \sqrt{\frac{2\epsilon_0 \epsilon_s E_{ft}}{q n_{D(x_p)}}}$$

Where E_{ft} is the trap energy level relative to the Fermi level of the semiconductor.

2.5 MARLOWE

MARLOWE is a simulation package available from Oak Ridge National Laboratory (U.S.A) [29] that uses a binary collision approximation to simulate atomic collision processes in crystalline solids. It is therefore well suited to simulate the implantation of ions into crystalline silicon and can predict the range of implanted ions as well as the concentration of vacancies left behind by displaced atoms.

Ion implantation for fabrication of the quantum computer is expected to require the use of low energy keV P ions. However, implantation of such ions does not place them, or the expected damage created from them at a suitable depth for analysis with DLTS. Therefore, a simulation package such as MARLOWE will be required to predict the defect concentration and defect profile.

2.6 Rutherford Backscattering-Channeling (RBS-C)

Channeled ions can also be used to determine the depth profile of lattice damage. In standard Rutherford Backscattering (RBS) light ions with MeV energies are fired into a sample and scattered with a certain energy

distribution depending on the constituents and structure of the sample. This is well described by elastic collisions between a fast moving light ion and a heavy stationary nucleus. It turns out that when the detector is placed at a small angle with respect to the surface normal of the sample good elemental resolution is obtained. However if ions are incident in channeling directions there will be a reduced yield of backscattered ions so standard RBS avoids channeling and operates in the random orientation.

If there is damage in the crystalline sample such as stacking faults or interstitial atoms then the channels will not be empty as in a perfect crystal (refer back to figure 2.1c). These atoms can then scatter any channeled ions and thereby increase the scattered yield and show up in the RBS-C spectrum as a a peak in scattered ion yield. This typically occurs if the atoms are displaced greater than 0.15 Å from a substitutional site [1].

As the incident ion collides with the atoms in the sample it looses energy. This is characterised by the kinematic factor (K) so that the final energy after collision is:

$$E_1 = KE_0$$

The kinematic factor depends only on the angle of the detector and the masses of the particles involved.

The ion will also lose energy on the inward and outward path principally due to inelastic interactions with the electron of the target. Hence the deeper the atom the ion finally scatters off the more energy it will lose. The final energy can now be written as [30]:

$$E_1(x_0) = E_2 - x_0 S$$

Where x_0 represents the depth of the scattering atom, S is the energy loss factor which encapsulates the attenuation of energy on inward and outward paths, and E_2 the energy of the ion had it scattered from an atom at the surface.

For a known initial energy of the ion it is possible to determine the depth of the target atom responsible for scattering the ion. So if this atom is in an interstitial location we have a mechanism for probing the depth of damage. With the increased yield giving information on the amount of damage and the energy range that this extends over indicating the range in depth the damage extends over.

Chapter 3

Experiment

3.1 Ion Implantation

The P implants were carried out on the Australian National University 1.7 MV NEC Tandem accelerator implanter (fig. 3.1a). An InP cathode was used which was sputtered with a Cs source to ionise the constituents. These were accelerated by electrostatic potentials in the extractor and P^- was selected by passing the beam through a 90^o magnet. The ion is then further accelerated by the terminal potential of the Tandem accelerator. To extract a positive beam the ion is stripped of an electron or electrons by N_2 gas bled into the centre of the terminal. For ion energies less than 100 keV however, the ion is not stripped of electrons and the accelerator is simply used to transport the ions through.

Along the beam line the ion beam passes through various sets of collimating slits that help confine the beam and limit divergence. This is important for the purposes of ion channeling since tight constraints are required for the angle of implantation.

To irradiate a sizable sample the beam is rastered over an aperture by X-Y scanners. This will add some divergence which has been calculated.

Due to the limited region that DLTS can probe for defects, the energy of implanted ions had to be carefully chosen to place the ions at a suitable depth. It was decided that a low energy 75 keV implantation would be performed to maintain some proximity to the energy regime to be adopted for constructing a quantum computer while creating defects deep enough to allow DLTS to probe the region beyond the projected range of implanted ions, as well as a higher energy 450 keV implantation to allow DLTS to probe the majority of defects created in the important region between the projected range of ions and the surface.

Pre-Implantation Cleaning

Samples were cleaned with methanol followed by acetone prior to implantation to remove excess hydrocarbons from the surface.

75 keV Implants

Room temperature substrate implants were performed with 75 keV phosphorus ions in two dose regimes, $1x10^{10}$ P/cm^3 and $5x10^{13}$ P/cm^3. The low dose regime was suitable for the requirements of DLTS while the high dose regime allowed sufficient damage to accumulate for RBS-C to be able to detect it. The implants were performed by rotating the sample 10^o away from the (110) axis and tilting the surface normal over angles of $0^o, 2^o, 4^o, 8^o$ and 12^o away from the incident ion beam. Implantations were performed over a 3x4 cm^2 aperture leading to a maximum divergence of less than 0.5^o. Samples were mounted with silver paint to ensure good thermal contact with the sample stage.

The first high dose samples were implanted with the substrate held at room temperature but no discernible damage could be found using RBS-C so low temperature substrate implants were then performed to eliminate room temperature self-annealing of defects created during the implantation process and hence to allow for a greater amount of damage being retained for RBS-C analysis. These implants were performed at angles of $0^o, 1^o, 4^o$, and 8^o. Samples were mounted with conductive carbon tape in this case.

450 keV Implants

Since the maximum implant angle for which ions will be channeled for 450 keV implants was expected to be much smaller than for the 75 keV case the exact angle the crystalline axis sits away from the surface normal of the polished wafer was determined by RBS-C prior to implantation. This was conducted on the University of

Melbourne Pelletron accelerator with 2 MeV He ions. The surface normal position was determined by passing a laser beam down the beam line and through a small aperture to reflect off the sample surface and aligning the sample so that the beam passed directly through the aperture. By performing RBS-C and measuring the yield at various sample tilts it was possible to locate the exact angle of the axial channel with respect to the surface normal. It was found to be 0.05^o from the surface normal for the wafer that was used for 450 keV implantations at the ANU.

In the ion implanter the surface normal had to be determined, once again using a reflected laser beam concentric with the ion beam. In this case, a second laser was also reflected from the implantation stage and projected on to a wall as some distance from the implant chamber to allow precise tilting of the stage (see fig. 3.1b). The beam divergence of the unrastered beam was measured to be 0.05^o and the raster scan contributed a further 0.1^o to the total divergence.

Implantations were performed at room temperature and at $0^o, 0.2^o, 0.5^o, 1^o$ and 2^o angles from the surface normal. Note that the 0.2^o implant was actually setup to be 0.25^o but only quoted to one significant figure owing to the limit to accuracy due to divergence. The ion dose was further restricted to 2x10^9 P/cm^{-3} since the higher energy ions in this case were expected to create more damage.

Implanted samples as well as two un-implanted (virgin) parts of the wafers used were then cleaved into 3x5 mm^2 chips. The virgin samples and set of samples implanted at different angles and energies were kept at room temperature while several other sets of the implanted samples were to be annealed.

3.2 Rapid Thermal Annealing

These samples were subjected to a single 15 minute rapid thermal anneal (RTA) in an Ar atmosphere. The RTA uses IR lamps to rapidly heat the samples at 100^oC/sec up to the desired temperature. RTA was performed at 200^oC, 300^oC and 400^oC. Samples were allowed to cool in the chamber before removal to cool in air until safe to handle. Samples typically spent no more than two minutes above 200^oC while cooling.

3.3 Electrical Contact Fabrication

To prepare the samples for electrical characterisation Schottky diodes needed to be fabricated on the surface. To facilitate the fabrication of reliable diodes samples had to be chemically cleaned. This consisted of a hydrocarbon clean by bathing in warm trichloro-ethylene (TCE) and isopropal-alcohol (IPA), followed by an immersion in 20% hydrofluoric acid (HF) to remove the native oxide on the surface. Following the HF etch samples were rinsed in de-ionised water and blow dried with nitrogen. They were then transferred immediately to the evaporation chamber to restrict rebuilding of the oxide.

Samples were placed over a mask with 0.6 mm circular apertures to allow the formation of Au contacts on the surface. The evaporation chamber was evacuated and pumped down to 5x10^{-6} torr before Au was resistively heated and evaporated through the mask.

Prior to measurement the ohmic back contact required was produced by application of an In/Ga eutectic to the back surface and scratched in with the blunt tip of a wire to break through the native oxide that would have now reformed.

The measurement stage consisted of a spring loaded needle contact to the Schottky diode and a flat metallic back plate for the ohmic back contact. This stage was then encased in a metal cap and inverted to be immersed in a liquid nitrogen bath. The temperature of the stage is monitored and controlled by varying the amount of the cap immersed in liquid nitrogen as well as with an electrical heater embedded in the base of the sample stage when necessary.

3.4 Electrical Measurements

C-V measurements were performed to examine the doping profile of the samples. This allowed evaluation of the quality of the Schottky diode such as the amount of leakage across the diode to determine the appropriate biases to use for measurement. C-V measurements also allowed setting the biases so that the DLTS scan region would be the same for each sample at room temperature.

DLTS measurements were performed with a 50 ms filling pulse, 10 ms measurement interval, with 6 windows of 20, 40, 80, 160, 320, and 640 ms length.

3.5 Ion Beam Analysis

RBS-C was carried out on the University of Melbourne's Pelletron accelerator. 2 MeV He ions were used for the RBS-C measurements to examine the amount of damage in the shallow surface region of 75 keV P implanted silicon. A virgin sample was analysed with channeled He ions in RBS-C in order to provide a control sample to compare the ion implanted samples to. This is important to correctly evaluate the amount of damage in the samples.

Displaced atom fractions were then extracted from the RBS-C spectra using the analytical code Nd which is based on the procedure outlined by Feldman et al. [31] and Zeigler [32].

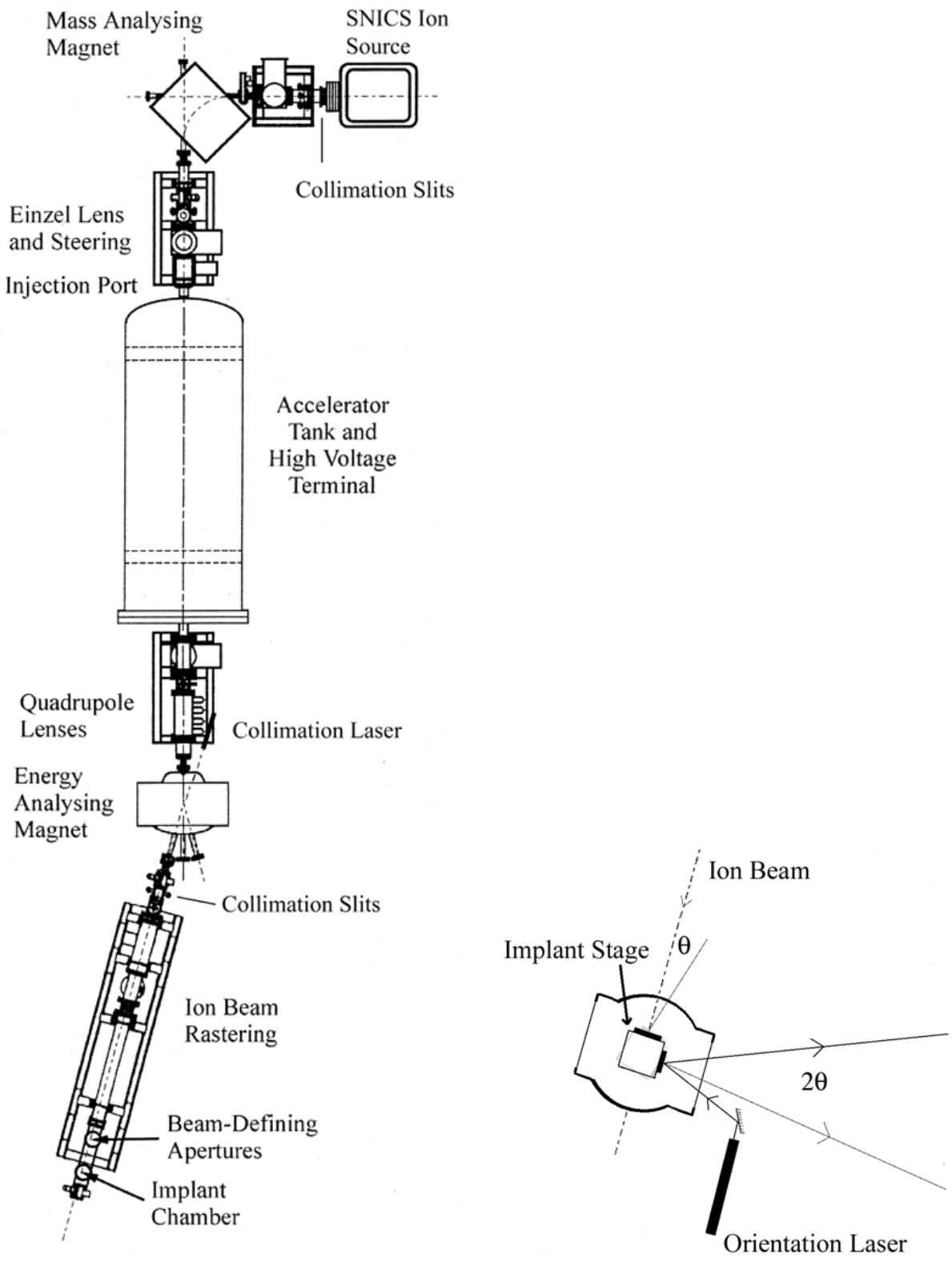

(a)

(b) Geometry for wafer orientation

Figure 3.1: 1.7 MV NEC Ion Implanter

Chapter 4

Results and Analysis

4.1 75 keV Implants

4.1.1 MARLOWE

The actual range of the implanted ions could not be experimentally determined due to the low dose of implantation. MARLOWE simulations were performed in place of this to predict the range of ions as well as an expected profile for the created vacancies.

Figure 4.1 shows the results of MARLOWE simulations for 75 keV P implants into (100) Si for channeled ions (θ=0^o), and for various tilts (θ=1^o-7^o) away from the (100) axis but parallel to the [110] planes. The effect of channeling implantation on the range of the P ions can be seen in figure 4.1a where the profile for channeled ions (open circles) is broad and ions have a projected range of about 0.5 μm. As the tilt is increased we can see that there are progressively less ions being channeled to a greater depth and that the projected range of ions shifts closer to the surface until it appears at about 0.1 μm which is the projected range for a random oriented implant. Note that once the tilt reaches 2^o there is a large change in the profile but for angles larger than this there is only a small shift in the projected range and for progressively larger angles there is little change at all. This shows that there is a criticle angle for channeling which for the case of 75 keV is predicted to be about 2^o. This result is a little smaller than previous values published in the literature using a simpler model [33, 34].

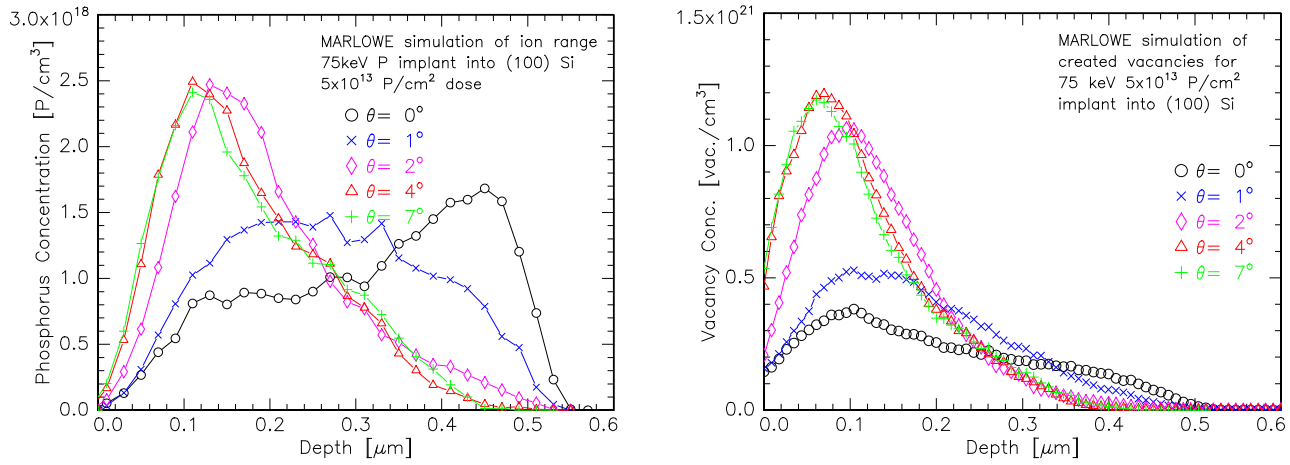

(a) Implanted P concentration

(b) Created Vacancy concentration

Figure 4.1: MARLOWE simulation of 75 keV implanted P at various angles

Figure 4.1b shows the corresponding profiles for generated vacancies as predicted by MARLOWE. The

channeled profile (open circles) now indicates that the peak region of vacancy production for 75 keV P implants is around 0.1 μm. Which interestingly, is well away from the projected range of channeled P at 0.5 μm. This is not the case for non-channeled ions and the predicted peak vacancy production region is quite close to the projected range of non-channeled ions at 0.1 μm.

The figure also shows that MARLOWE predicts that the maximum created vacancy concentration increases with implantation angle. These results indicate that channeled implantation may therefore be a method of implanting ions with a reduced total concentration of vacancies as well as a reduced concentration near the range of the implanted ions. DLTS can be performed to evaluate whether these predictions adequately represent reality.

4.1.2 DLTS

Channeling Study

Figure 4.2 shows the DLTS spectra obtained for implanted samples at various angles. Each spectrum is the result of a DLTS scan for a sample implanted at a different angle. The spectra show four primary peaks (P1-P4) corresponding to the electrically active traps in the samples. These spectra are consistent with what has been reported in the literature for ion implanted n-Si.

The spectrum presented is a plot of data from an 80 ms measurement window. This window was chosen to reveal the defect peak at low temperature (P1) which is shifted to even lower temperatures with larger measurement windows.

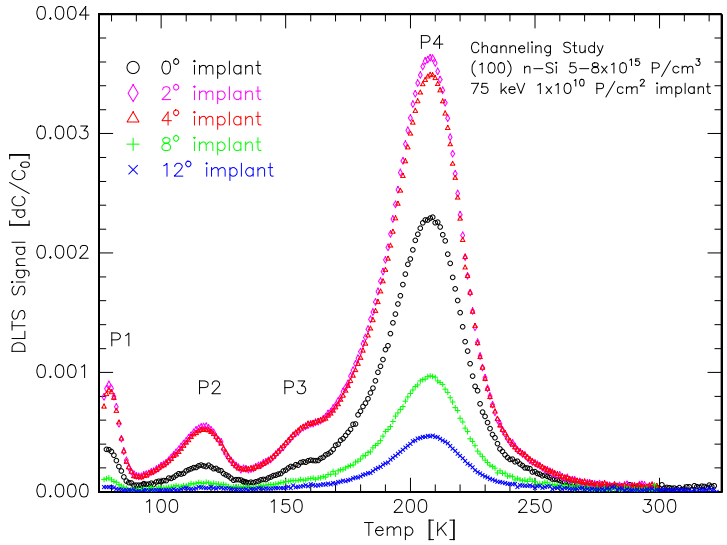

Figure 4.2: DLTS spectra obtained from 80 ms measurement window for 75 keV implants at various angles.

Peak heights are proportional to defect levels (c.f. eq. 2.8) so from figure 4.2 it can be seen that although samples seem to have the same species of defects present they have differing concentrations.

DLTS was also performed on the virgin sample but no defect peaks were observed indicating that defect peaks observed for implanted samples are indeed due to ion implantation related defects (see Appendix A figure 6.4).

The defect peaks in the spectra have been analysed to determine the characteristics of the defects. These are shown in table 4.1 along with their likely identity based on their characteristics. Quoted values are the calculate averages for the results and errors indicate the range of values obtained.

Although P1 and P3 could not be analysed they have been identified as the VO center and VO-H center respectively since they have peak temperatures close to what would be expected for these defects, and also because the VO and VO-H are commonly found defects in ion-implanted n-Si (refer to references for these in table 2.1.

Defect label	Energy level [eV]	Capture cross–section [cm^2]	Possible Identity
P1	–	–	VO
P2	$E_c - 0.23 \pm 0.01$	$(3\pm2)x10^{-15}$	V_2^{2-}
P3	–	–	VO-H
P4	$E_c - 0.43 \pm 0.02$	$(5\pm3)x10^{-15}$	VP/V_2^-

Table 4.1: Characteristics of defects found in 75 keV $1x10^{10}$ P/cm^2 as–implanted samples.

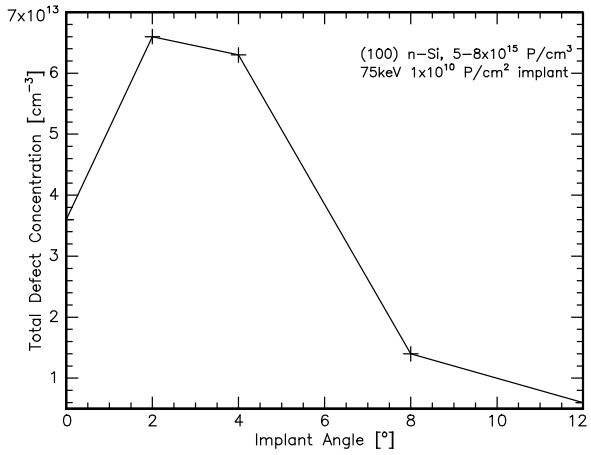

Figure 4.3: Plot of defect concentrations as a function of angle for 75 keV implants.

The defect concentrations were also calculated using equation 2.10, taking the average value for the carrier concentration and using DLTS signal data from the largest measurement window (640 ms). It is important to take data from the largest measurement window for calculations because the capacitance changes over time until some equilibrium is reached and it is the total change in capacitance that is representative of the true defect concentration.

Since the VO peak (P1) is not present in the 640 ms window, however, it was necessary to scale its value to approximate what its true value might be with the 640 ms window according to how the other defect peak signals scale.

Figure 4.3 shows the total concentration of defects measured in the DLTS probe region between 0.41 μm and 0.81 μm as a function of implantation angle. This total concentration of defects was calculated from the sum of individual defect concentrations. The variation in concentration with angle for each individual defect shows a similar behaviour to that shown in figure 4.3.

From figures 4.2 & 4.3 we find that the samples implanted with 75 keV P at 2^o and 4^o have the largest measured concentration of defects, and that the 0^o has the next largest concentration. This clearly does not match up with the predictions of the MARLOWE simulations, however this may not be too surprising since the effects of Frenkel defect recombination and defect migration aren't taken into account by the code.

If we consider that MARLOWE predicts the correct initial distribution and concentration of defects for the implants though, the following explanation of results may be entertained. MARLOWE predicts that in the 2^o and 4^o implanted samples less defects are created than the 8^o and 12^o but the defects are created deeper, this may therefore lead to a greater concentration of defects diffusing into the deep DLTS probe region. MARLOWE also predicted that the 0^o creates the least defects but has the deepest range. This may explain why it has more measured defects than the 8^o and 12^o samples.

However, we must also consider these that results do not represent the total concentration of defects introduced since we are probing a region well beyond where the expected peak of vacancy production is. Despite this, it is clear that even at these depths beyond the projected range of ions there is a substantial concentration of defects present.

To explore this point further we may use the present result to calculate a lower limit for the efficiency of damage production. If we consider that a channeling implant of $1x10^{10}$ P/cm^2 is spread over a 450 nm depth (as seen from MARLOWE simulations fig. 4.1a) we obtain an average implanted ion concentration of

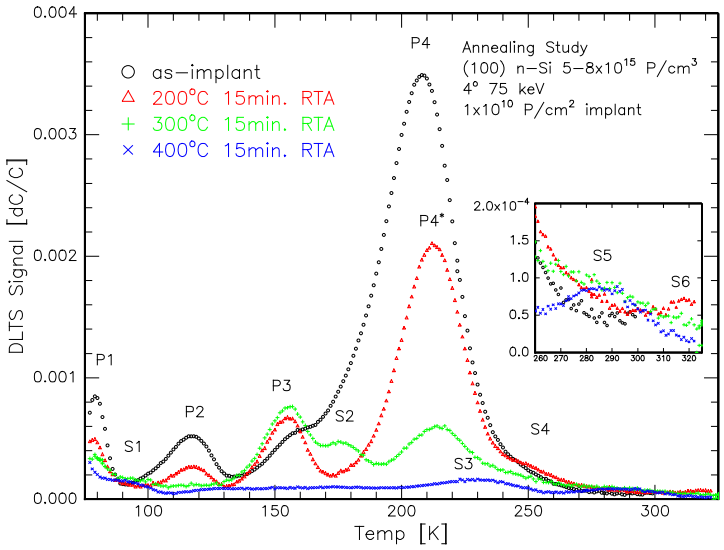

Figure 4.4: DLTS spectra obtained from 80 ms measurement window for 75 keV 4^o implanted samples annealed for 15 min. at various temperatures.

$2.2\text{x}10^{14}$ P/cm^3. Comparing this with the values in figure 4.3 it seems as if there are at least between 10 and 100 implanted ions per defect projected into the DLTS probe region.

It is not clear whether figure 4.3 indicates that the defect concentrations have this behaviour over the entire sample or just in the region being probed until the concentration of defects in the near surface region is examined since this is where the peak vacancy production is meant to be.

Isochronal Annealing Study

The response of samples implanted at different angles upon annealing are fairly similar to each other and only plots for the 4^o implanted samples are shown here (figure 4.4), the complete set of DLTS plots can be found in Appendix A.

Figure 4.4 shows that as the sample is annealed most defects are reduced (VO & VP/V_2^-) but the VO-H peak increases and new secondary defects also appear (S1-S6). Since the annealed samples enable the VO-H to be resolved it can now be analysed along with other secondary defects. The averaged values for their energy levels and capture cross-sections are shown in table 4.2. The annealing behaviour of these defects along with their possible identity as established by comparing defect characteristics with those quoted in table 2.1 and table 2.2 is shown in table 4.3.

Figure 4.5a plots the concentrations of the primary defects as a function of annealing temperature. Concentrations have been determined as mentioned on page 18. Samples implanted at other angles have a similar behavior.

There are two features from these figures that illustrate the complex behavior of defects. The first is that all of the defects decrease in concentration except for P3 (VO-H) (see fig. 4.5a). The second is the appearance of secondary defects after anneals over 200^oC (eg. 300^oC data in fig. 4.4 (green plus signs)). These effects are consistent with data shown in table 2.2 and occur as a result of constituents of some primary defects being freed as the defect dissociates and having these constituents bonding with other defects or clustering to form new stable complexes [24].

Figure 4.5b shows the annealing behavior of the total defect concentration of samples implanted at various angles. When the ratio of final defect concentration to initial defect concentration after a 400^oC is performed

Defect label	Energy level [eV]	Capture cross–section [cm^2]
P1	–	–
S1	–	–
P2	$E_c - 0.23 \pm 0.01$	$(3\pm2)x10^{-15}$
P3	$E_c - 0.30 \pm 0.01$	$(2\pm1)x10^{-15}$
S2	$E_c - 0.35 \pm 0.01$	$(5x\pm4)x10^{-15}$
P4	$E_c - 0.43 \pm 0.02$	$(5\pm3)x10^{-15}$
P4*	$E_c - 0.49 \pm 0.03$	$(3\pm2)x10^{-16}$
S3	$E_c - 0.49 \pm 0.01$	$(2\pm1)x10^{-15}$
S4	–	–
S5	$E_c - 0.59 \pm 0.01$	$(4\pm1)x10^{-15}$
S6	–	–

Table 4.2: Characteristics of defects found in annealed 75 keV $1x10^{10}$ P/cm^2 implanted samples.

Defect label	Reverse Annealing Temperature [^oC]	Annealing Temperature [^oC]	Possible Identity
P1	–	400+	VO
S1	300	400+	V-related (0.19 eV)
P2	–	300	V_2^{2-}
P3	200	400	VO-H
S2	300	400	V-related
P4	–	200	VP/V_2^-
P4*	–	400	V_2^-
S3	–	400+	–
S4	200	300	–
S5	400	400+	–
S6	200	300	–

Table 4.3: Annealing behaviour of defects found in annealed 75 keV $1x10^{10}$ P/cm^2 implanted samples.

we find that the channeled implanted ions are reduced by a factor or about 9 and implants at higher angles are reduced by a gradually reducing factor with the 12 degree implant only being reduced by a factor of 4 after a 15min 400^oC RTA.

Figure 4.5b also shows that the lines never cross indicating that the only way of ending up with a smaller concentration of defects after RTA in comparison with another sample is to begin with a smaller amount. This is to say that the effectiveness of RTA is independent of samples.

Since the DLTS probe region is much deeper than where most defects are expected to be produced it could be argued that the results obtained may be misleading since the defects may have simply migrated beyond the probe region. However, it has been noted that the defect profile does not change much in terms of it's shape upon annealing [21]. This means that the results obtained in this probe region are expected to be representative of the total change of the defect concentration.

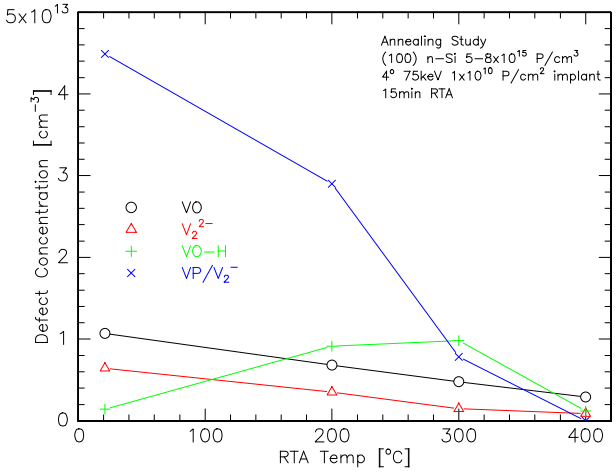

(a) Annealed 4^o implanted samples

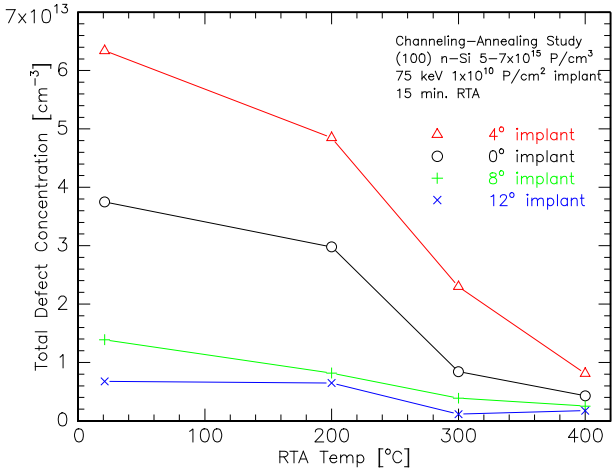

(b) Total concentration of annealed samples implanted at various angles

Figure 4.5: Annealing behaviour of defects for 75 keV implanted samples annealed for 15 min.

4.1.3 RBS-C

RBS-C has been used to examine the amount of damage in silicon kept at liquid nitrogen temperatures while being implanted with 75 keV P in order to gain some insight into the defect/damage production over the full range of the implanted ions as a functio of implantation angle. Results obtained from RBS-C experiments were analysed with the Nd program to determine the depth profile of damage shown in figure 4.6, the raw spectra can be found in Appendix B. The figure indicates the fraction of silicon at a particular depth that is displaced from its substitutional lattice position. The large peak near the surface is due to scattering from the first few mono-layers of silicon at the surface.

We see that indeed there does seem to be more damage for larger angle implantations (blue cross, green plus) and that they also have a shallower range than the channeled ion implanted sample (open circles). This is consistant with what MARLOWE predicts for the vacancy depth profile although the peak depth for damage is a little shallower. This result is a little surprising considering that the damage profile calculated from RBS-C is often more of a closer match to the implanted ion depth profile since it is where the ion stops that most damage leading to interstitial atoms or other lattice damage is expected.

Although RBS-C does not directly tell us about the number of vacancies in the substrate. One would expect that if there are mostly interstitial atoms giving rise to an increased back scattered ion yield in the RBS-C signal then there must be accompanying vacancies somewhere. These results therefore add fuel to the fire indicating that MARLOWE correctly predicts that larger implantation angles should result in more vacancies. However, we must be wary of the fact that since the 75 keV P implants for RBS-C analysis were performed at low temperatures they will automatically be more closely correlated to MARLOWE predictions (which is essentially modelling a T= 0 K substrate). How implantation into a room temperature substrate changes things cannot be explained with either RBS-C or MARLOWE. Only a direct examination of the region where the majority of vacancies are in room temperature implanted silicon can reveal this. The 450 keV implants go someway towards addressing this issue.

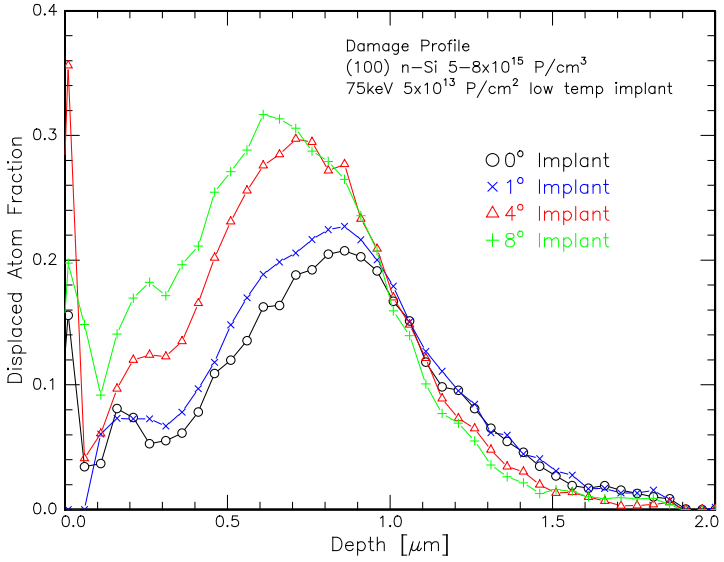

Figure 4.6: Depth profile of damage as determined from RBS-C data for samples implanted at 400°C with 75 keV P at various angles.

4.2 450 keV Implants

4.2.1 MARLOWE

MARLOWE simulations were also conducted for 450 keV P implantation into (100) silicon for channeled ions and various tilts away from the (100) axis. These are shown in figure 4.7a and 4.7b. The ions stop being channeled when they are more than 0.5^o off axis. This indicates that the channeling window is reduced when ion energy is increased. These non-channeled ions are predicted to have a projected range of 0.6 μm accompanied by a peak in vacancy production around this depth. The channeled ions also seem to show a peak in vacancy generation at this depth while the ions have a projected range of about 1.6 μm. The defects in the important region between the ions and the surface can now be probed with DLTS.

Once again MARLOWE predicts that the created vacancy concentration should also increase with implantation angle and that there should be a shift in the peak depth towards the surface as well.

4.2.2 DLTS

Channeling Study

Figure 4.8 shows the DLTS spectra obtained for the 450 keV implanted samples at various angles, once again showing the data from the 80 ms window. Again the spectra reveal that samples have the same species of defects present with the exception of the 2^o implant which has an extra defect labelled P5. This is likely to be a peak from a contaminant introduced during the diode fabrication step, possibly a metallic impurity, since previously, contaminated samples prepared from the same implanted chip revealed a large defect peak in this region.

A virgin sample taken from the same wafer that implanted samples were from was scanned with DLTS and once again did not reveal any defect peaks in the scan (see Appendix C figure 8.4).

Defect peaks have once again been analysed and results for defects observed in as–implanted samples are shown in table 4.4. As can be seen from the table, aside from P5, the 450 keV implants also have the same defects as found with the 75 keV implants. This provides some indication that there is little energy dependence for the types of species introduced into the sample, which is important if results are to be extrapolated down to low energies as needed for the quantum computer.

Referring back to figure 4.8 the samples differ in the concentration of each defect but the ratio between defects is much different now in comparison to the 75 keV samples. For example, P4 for the 2^o implanted sample (green plus) has an intermediate concentration but P2 for the 2^o has the lowest concentration in comparison with the other samples. This is an effect that was not observed in the scans for the 75 keV implanted samples,

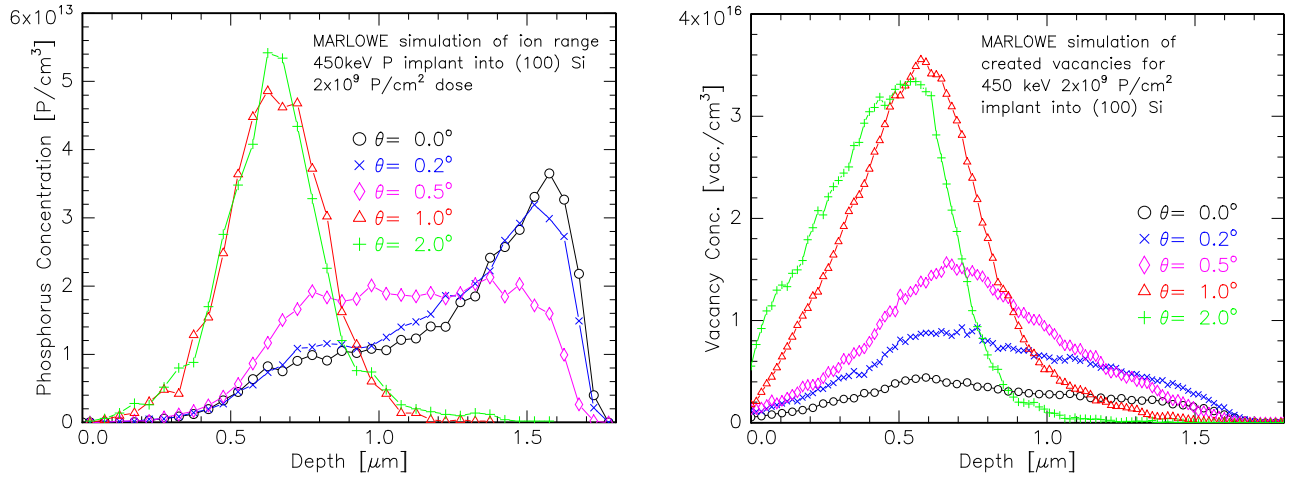

(a) Implanted P concentration

(b) Created Vacancy concentration

Figure 4.7: MARLOWE simulation of 450 keV implanted P at various angles.

Defect label	Energy level [eV]	Capture cross–section [cm^2]	Possible Identity
P1	–	–	VO
P2	$E_c - 0.22 \pm 0.01$	$(1.2 \pm 0.4) \times 10^{-15}$	V_2^{2-}
P3	–	–	VO-H
P4	$E_c - 0.42 \pm 0.01$	$(4 \pm 3) \times 10^{-15}$	VP/V_2^-
P5	–	–	Metallic Impurity

Table 4.4: Characteristics of defects found in 450 keV 2x10^9 P/cm^2 as–implanted samples.

where the order of largest to smallest defect concentrations was consistent for all the defect peaks. A possible explanation of this is that the DLTS probe region varies with temperature from sample to sample which would affect the calculated concentration of defects. Analysis has revealed that the extent of this is limited to about 80 nm difference between samples in the 0.4 μm region. This will have a greater affect in comparison with the 75 keV samples now because the defect peaks are expected to be around this region, i.e. a small change in depth can result in a larger change in defect concentration than before. It is unclear however whether the extent of this is enough to account for the discrepancies mentioned above. It may also be that the 2^o implant simply preferentially produces or results in the production of more of the P4 type defect. Defect depth profiles can potentially resolve this issue.

Concentrations of defects have been calculated as mentioned on page 18 and the total defect concentration have been plotted as a function of implant angle in figure 4.9.

From figure 4.9 we see that the defect concentration is now increasing with implantation angle up until the 0.5^o implant. So, once again the DLTS scans seem to indicate a criticle angle for defect production. This result potentially rules out the idea oulined earlier in this report that this angular dependence may only apply to defects that migrated beyond the projected range of the ions. It would be useful to examine samples at larger number of angles to explore this effect further.

Re-examining the implanted ion profiles predicted by MARLOWE (fig. 4.7a) we see that the ions are implanted over a range between the surface and up to 1.8 μm for channeled ions. Note that the 0.5^o implanted ions (pink diamonds) are predicted to have a similar ion range as the channeled ions (open circles). For our implanted dose of 2x10^9 P/cm^2 then gives an average implanted ion concentration of about 2x10^{13} P/cm^3. Figure 4.9 shows that we have a least 7x10^{13} defects/cm^3 for the channeled ions (implant angle of 0) and 1x10^{13} defects/cm^3 for the 0.5^o implant angle. This indicates that we have between 1 and 4 stable defects created per implanted ion.

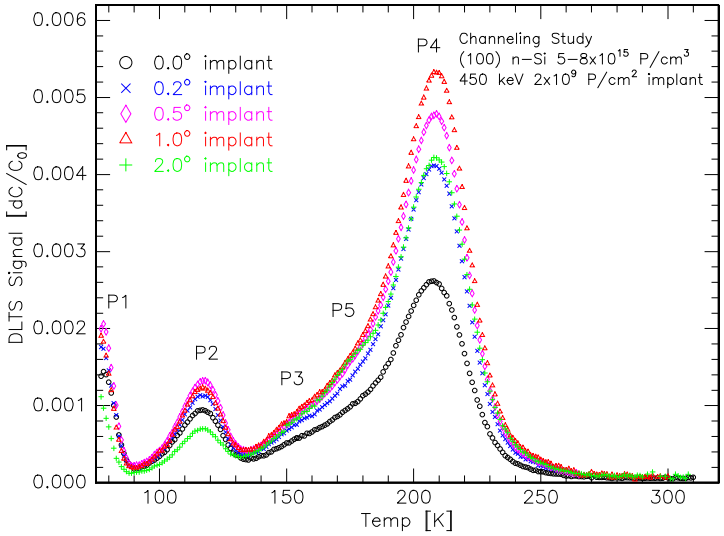

Figure 4.8: DLTS spectra obtained from 80 ms measurement window for 45 keV implants at various angles.

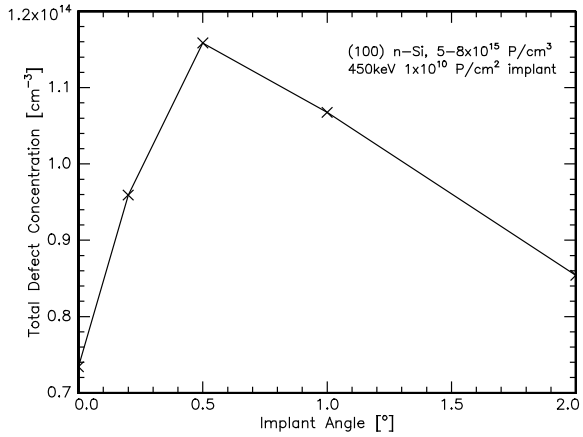

Figure 4.9: Plot of defect concentrations as a function of angle for 450 keV implants.

Isochronal Annealing Study

The results of DLTS scans of annealed samples revealed similar behaviour between samples implanted at various angles and only the plots for the 1^o implanted samples are shown here (figure 4.10), the complete set of DLTS plots can be found in Appendix C. The main discrepancy found was with the annealing behaviour of the doubly charged divancy (P2, V_2^{2-}). It was found that for the 2^o implanted sample the V_2^{2-} was observed to have a reverse annealing behaviour and grow in concentration upon a 200^oC anneal (see later fig. 4.12b). The 0^o implanted sample revealed no change in the V_2^{2-} concentration and the 1^o sample shown in figure 4.10 and figure 4.12a shows the P2 peak being annealed out as expected. The reasons for this behaviour are unclear.

This set of samples also displayed different annealing behaviour to the 75 keV set in that less secondary defects are observed. Without having any knowledge of the possible nature of these secondary defects, it is difficult to put forward any argument as to the reason for this difference.

The defects observed in annealed samples have been analysed and the results appear in table 4.5. These values are in broad agreement with the results found in table 4.2 for 75 keV implants. The annealing behaviour of these defects along with their possible identity as established by comparing defect characteristics with those quoted in table 2.1 and table 2.2 is shown in table 4.6

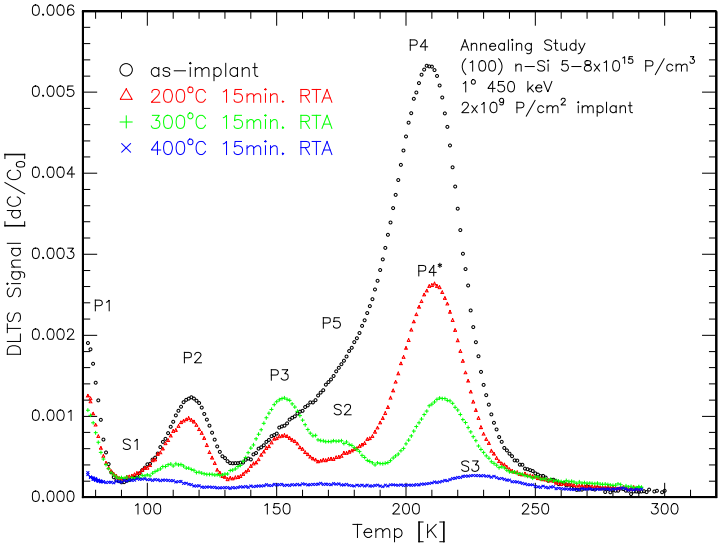

Figure 4.10: DLTS spectra obtained from 80 ms measurement window for 450 keV 1^o implanted samples annealed for 15 min. at various temperatures.

Defect label	Energy level [eV]	Capture cross–section [cm^2]
P1	–	–
S1	–	–
P2	$E_c - 0.21 \pm 0.01$	$(1.2\pm0.6)x10^{-14}$
P3	$E_c - 0.29 \pm 0.02$	$(3.2\pm2.5)x10^{-14}$
S2	$E_c - 0.34 \pm 0.01$	$(1.0\pm0.9)x10^{-15}$
P4*	$E_c - 0.45 \pm 0.02$	$(2\pm1)x10^{-15}$
S3	$E_c - 0.45 \pm 0.01$	$(8\pm2)x10^{-15}$
S4	–	–

Table 4.5: Characteristics of defects found in annealed 450 keV 2x10^9 P/cm^2 implanted samples.

The annealing behaviour of each of the defects identified in the 0^o, 1^o and 2^o implanted samples have been plot in figures 4.11 & 4.12a. The results for the 0^o & 1^o implantes sample are in agreement with the annealing behaviour for these defects presented for the 75 keV implanted samples as well as those published in the literature (refer to table 2.2. However the 2^o case is not in agreement since the VO trap increases in concentration. This could be an indication that there is excess oxygen in the sample which is not in a complex with a vacancy until the release of vacancies from the divacancies provides more vacancies to form the VO.

The plot of the annealing behaviour of total concentration of defects as calculated for the 0^o, 1^o and 2^o implants however are much different to those in the 75 keV case (fig. 4.5b). By once again comparing the initial concentration of defects to that remaining after the 400^oC 15min. RTA we now find that all of the samples show a reduction by factors of 8.5, 8.2 and 9 for the 0^o, 1^o and 2^o implants respectively. This agrees with our expectations that the effectiveness of annealing should not depend on the angle of implant since the same species of defects are observed in each case. This would seem to suggest that the previously calculated values for the 75 keV implanted samples are simply a result of only probing the deep region beyond the projected range of the implanted ions.

The annealing behaviour of the 2^o implanted sample (green plus signs) was completely unexpected in that it shows that the total concentration of defects did not decrease upon annealing up to 300^oC. This behavior is not obvious from just an examination of the DLTS spectra since the value for the average doping concentration ,ist a;sp be taken into account when evaluating the defect concentration (see eq. 2.10).

That the total concentration of measured defects does not significantly decrease with annealing in the 2^o implanted sample could be an indication that there are other defects present that dissociate to then contribute to the the VO and VO-H defects, which can be seen to increase in concentration upon annealing (fig. 4.12a).

Defect label	Reverse Annealing Temperature [^{o}C]	Annealing Temperature [^{o}C]	Possible Identity
P1	–	400+	VO
S1	400	400+	V-related (0.19 eV)
P2	–	400	V_2^{2-}
P3	300	400	VO-H
S2	300	400	V-related
P4	–	200	VP/V_2^-
P4*	–	400	V_2^-

Table 4.6: Annealing behaviour of defects found in annealed 450 keV 2x10^9 P/cm^2 implanted samples.

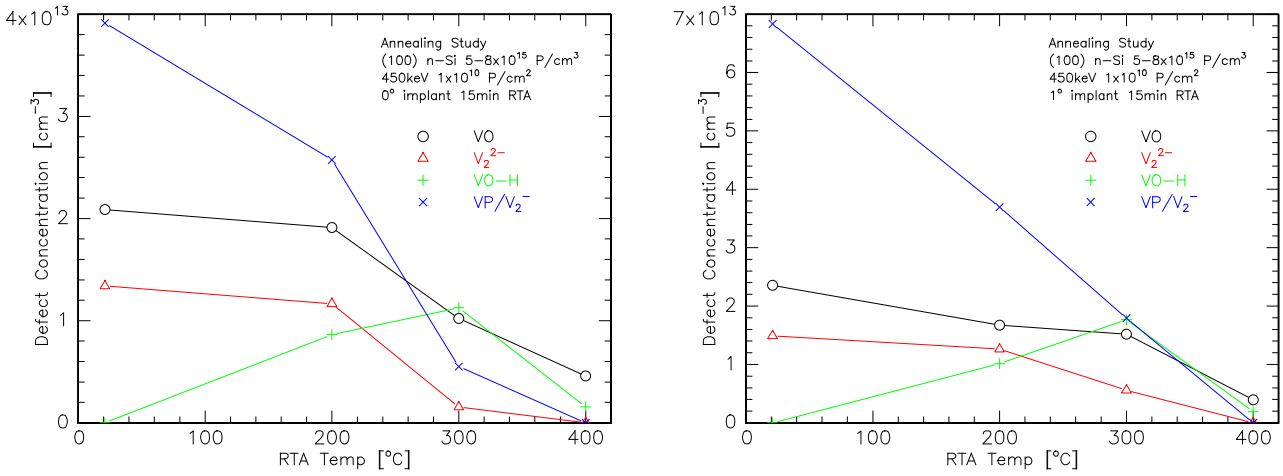

(a) Annealed 0^o implanted samples

(b) Annealed 1^o implanted samples

Figure 4.11: Annealing behaviour of defects for 450 keV implanted samples annealed for 15 min.

Since the divacancy is seen to decrease in concentration it could be that as the divacancies anneal out, what was two vacancies forming one defect dissociates to complex with two oxygens to form two new defects, thus this could be a mechanism for the formation of two defects for the price of one. Clearly the annealing behaviour is not completely understood and needs to be explored in more detail.

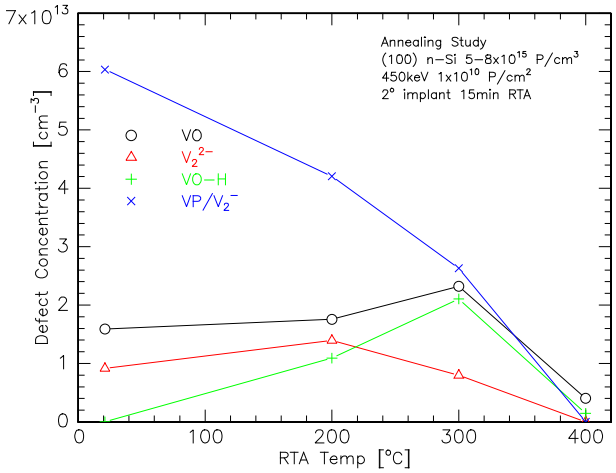

(a) Annealed 2^o implanted samples

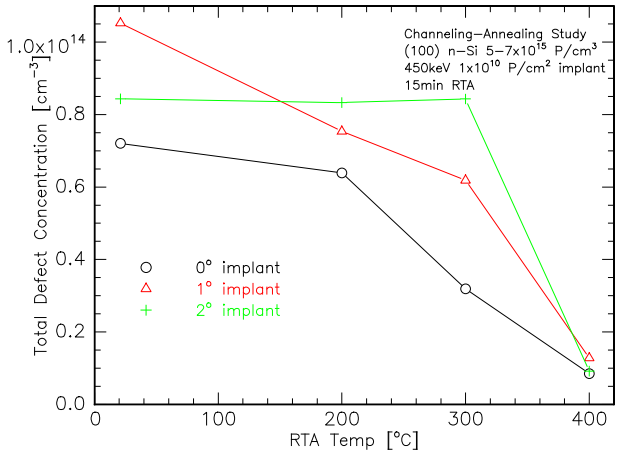

(b) Total concentration of annealed samples implanted at various angles

Figure 4.12: Annealing behaviour of defects for 450 keV implanted samples annealed for 15 min.

4.2.3 Depth Profiles

The depth profiles do not suffer from the issue of the scan region changing with temperature because they are isothermal measurements and also associate a depth for each result obtained for the defect concentration. It can therefore potentially clear up the issue as to whether the DLTS scans are providing consistent data for the calculation of defect concentrations and the subsequent comparison between samples.

The results from depth profiling the P1-P3 defect peaks as seen in the DLTS spectra were quite noisy and only defect profiles of the P4 (VP/V_2^-) peak are shown here. Note that each data point is average over many scans and the remaining scatter in results indicates the level of noise.

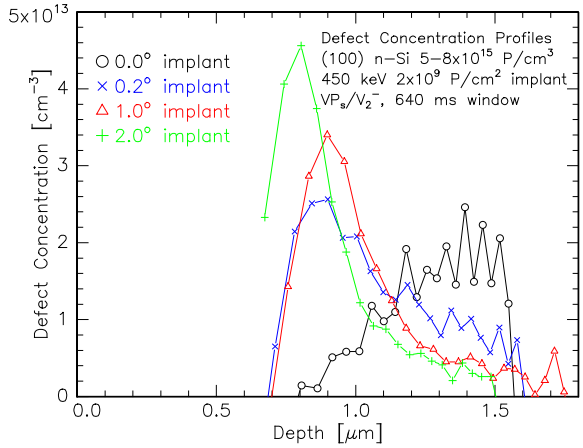

Figure 4.13: Plot of $[VP/V_2^-]$ depth profile for samples implanted with 450 keV P at various angles.

Figure 4.13 shows the depth profiles obtained for the VP/V_2^- defect from as–implanted samples, profiles for other defects can be found in Appendix D. The most striking feature of this is that the 0^o implanted sample (open circles) is vastly different to those observed for larger implant angles. This is contrary to what is predicted from MARLOWE for the vacancy profile (see fig. 4.7b). However, the depth profiles clearly show that the peak defect concentration increases with implantation angle as MARLOWE had predicted though. The other feature in agreement with MARLOWE is that the non-channeled spectra also result in defect peaks closer to the surface

with larger implantation angles.

There is a possible means of reconciling the observed defect profiles with the vacancy generation profiles predicted by MARLOWE. It has been published in the literature that the surface region can act as a sink for defects and proximity to the surface can enhance Frenkel defect recombination [35, 36]. If this is the case and the number of defects being annihilated the reduces with depth (perhaps at first guess an inverse relationship between number of defects annihilated and depth), then by subtracting this amount out of the predicted MARLOWE profiles it may be possible to obtain a similar profile to what was experimentally measured. This concept would require a greater investment of time to fully explore.

Figures 4.14 & 4.15 show the response of the defect profiles obtained for the V_2^- defect upon annealing for the 0^o and 2^o implanted samples respectively. Profiles for other defects can be found in Appendix D.

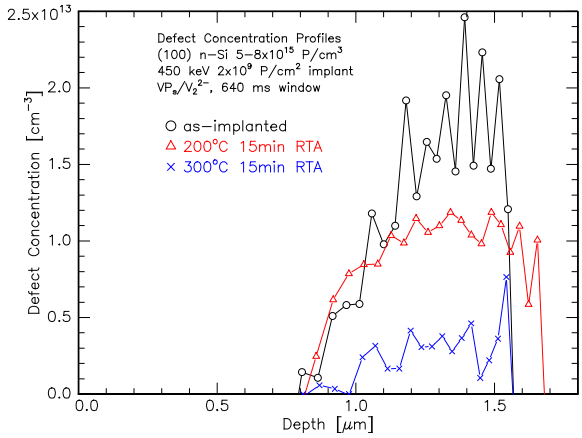

Figure 4.14: Plot of $[VP/V_2^-]$ depth profile for samples implanted with 450 keV P at 0^o and annealed for 15 min.

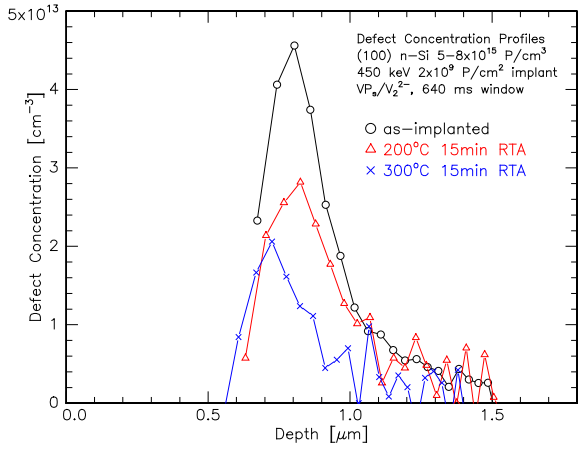

Figure 4.15: Plot of $[VP/V_2^-]$ depth profile for samples implanted with 450 keV P at 2^o and annealed for 15 min.

Figure 4.14 importantly shows that the profile shown in figure 4.13 for the channeled implant sample was not an isolated case and that the shape of the profile is maintained over annealing up to 300^oC. The fact that the defect profile doesn't change shape upon annealing has been previously published in the literature [21].

From figure 4.15 it can be seen that upon progressively higher temperature anneals more defects are removed from the region of greatest concentration.

Chapter 5

Conclusions and Further Work

The DLTS analysis performed on P as–implanted n–Si in this project revealed that a non–trivial number of vacancy–related defects were produced. In the 75 keV energy regime that examined the depth region beyond the projected range of the implanted ions it was found that between 0.1 and 0.01 defects per cm^3 was detected per implanted ion per cm^3. It is recognised that this represents a lower limit to the expected true value since MARLOWE predicted the region of peak vacancy production to be near the projected range of the implanted ions. Further analysis of 450 keV P as–implanted samples revealed that by probing the region between the surface and the projected range of the ions that figures closer to between 1 and 10 defects remaining per cm^3 for every implanted ion per cm^3.

The DLTS results also show that measurable trap concentrations still exist after 400^oC 15 min. RTA and that higher temperatures will be required for the quantum computer. The efficiency of the annealing procedure was found to be largely independent of implant angle for the 450 keV implanted samples where it was found that initial concentrations of defects were reduced by roughly an order of magnitude. The 75 keV implanted samples initially indicated that more defects were removed from channeled implanted samples however this is to be treated as suspect due to the fact that the majority of defects were not capable of being examined with these samples.

The angular dependence of heavy ion implanted silicon had not previously been examined before. As a result of this work, it has been established that the same species of defects were present in all implanted samples independent of the angle of implantation and that the only difference between samples seemed to be the concentrations of each defect and their depth distribution.

Although DLTS seemed to indicate there being a critical angle for defect production (curiously closely correlated to the critical angle for ion channeling) subsequent analysis of 75 keV implants with RBS-C and DLTS depth profiling of 450 keV implanted samples revealed no such effect. Moreover these two methods of depth profiling damage and defects revealed a close correlation with the expected vacancy production as predicted by MARLOWE and confirms that channeled ions indeed produce less defects than implants at larger angles. The important difference however is that channeled implanted ions do not produce the defect distribution predicted by MARLOWE but create a peak in defect concentration that is much deeper than predicted. In particular the large offset between the peak vacancy depth and the projected ion range as predicted by MARLOWE is not supported by the DLTS results. It is not clear at this stage whether the predictions from MARLOWE can be fully reconciled with the DLTS measurements.

This project has re–iterated the fact that the world of defect studies is rich with complexity. As it were there are many interesting effects that at present do not have an adequate explanation. The inconsistencies in the annealing behavior of the 450 keV implanted samples for example may be studied further. In particular the source of defects that lead to an observed reverse annealing effect for the VO centre may be explored in greater detail. The reason why DLTS data consistently seemed to suggest the existence of a critical angle for maximum defect production also needs to be identified. The realisation that DLTS depth profiles can be a much more reliable and powerful tool in examining the defect levels of semiconductors leaves plenty of hope for future studies in this area.

Chapter 6

Appendix A- DLTS Spectra for Annealed 75 keV Implanted Samples

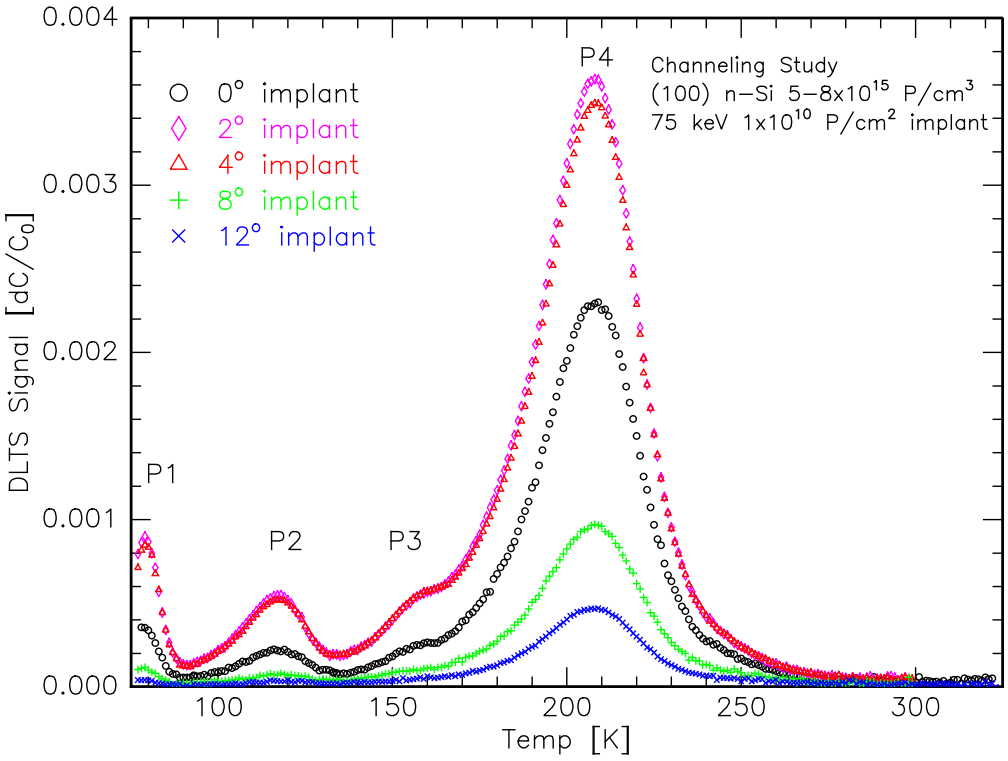

Figure 6.1: DLTS spectra obtained from 80 ms measurement window for 75 keV implanted samples.

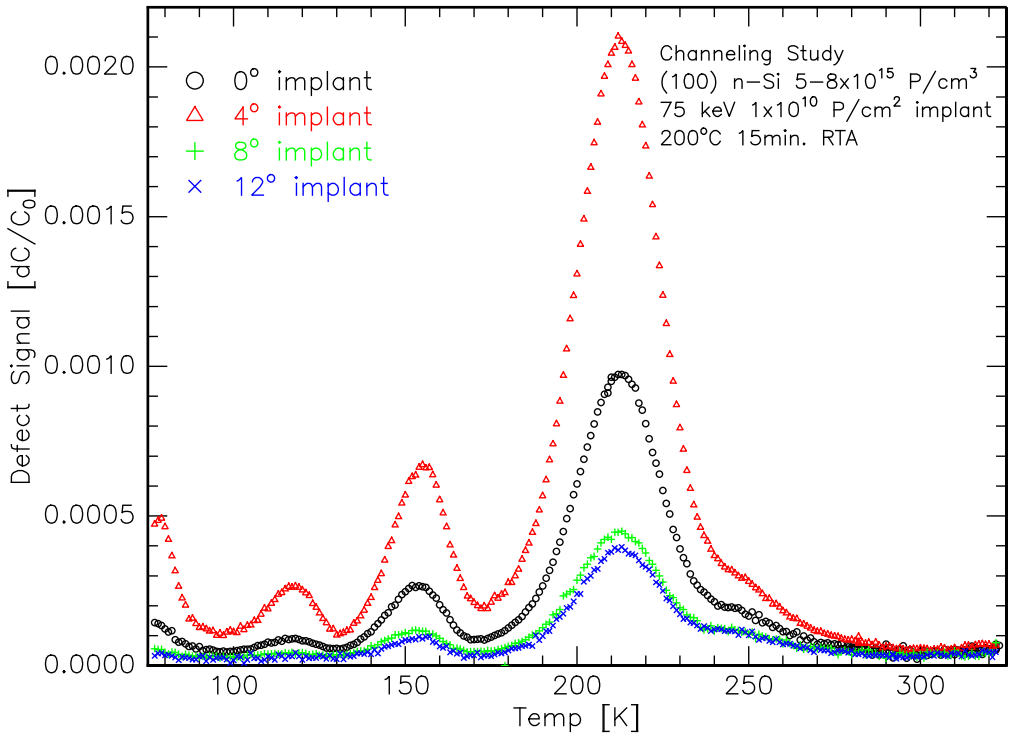

Figure 6.2: DLTS spectra obtained from 80 ms measurement window for 75 implanted samples Rapid Thermal Annealed for 15 min. at 200^{o}C.

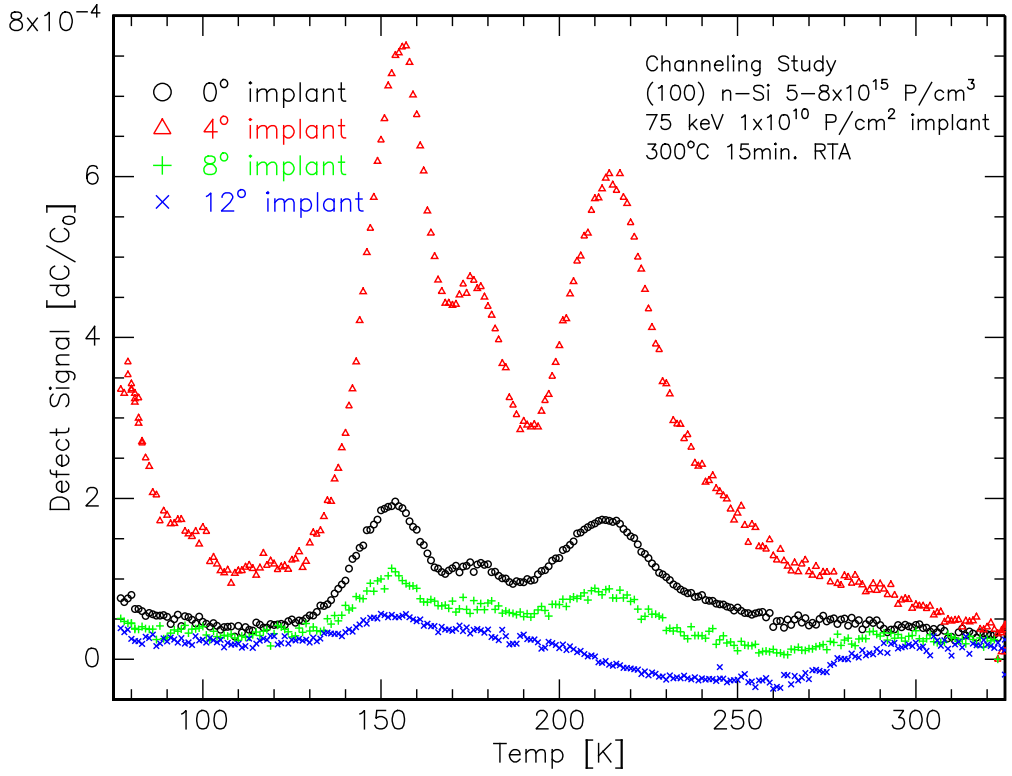

Figure 6.3: DLTS spectra obtained from 80 ms measurement window for 75 implanted samples Rapid Thermal Annealed for 15 min. at 300^{o}C.

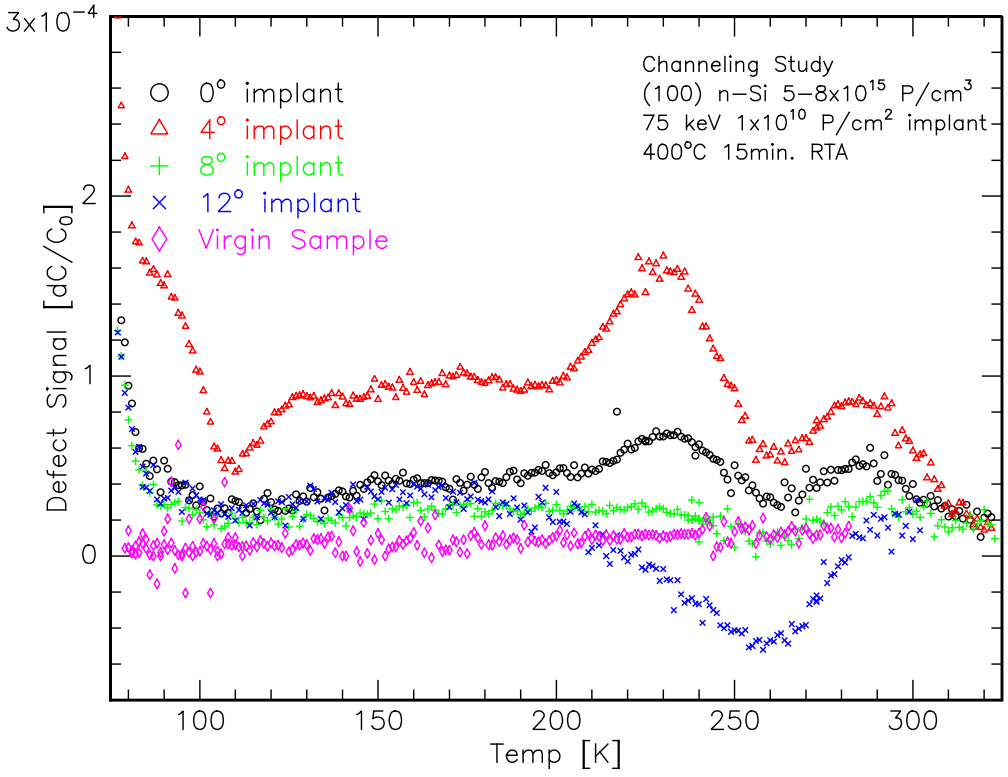

Figure 6.4: DLTS spectra obtained from 80 ms measurement window for 75 implanted samples Rapid Thermal Annealed for 15 min. at 400^{o}C.

Chapter 7

Appendix B- RBS-C Spectra for 75 keV Implanted Samples

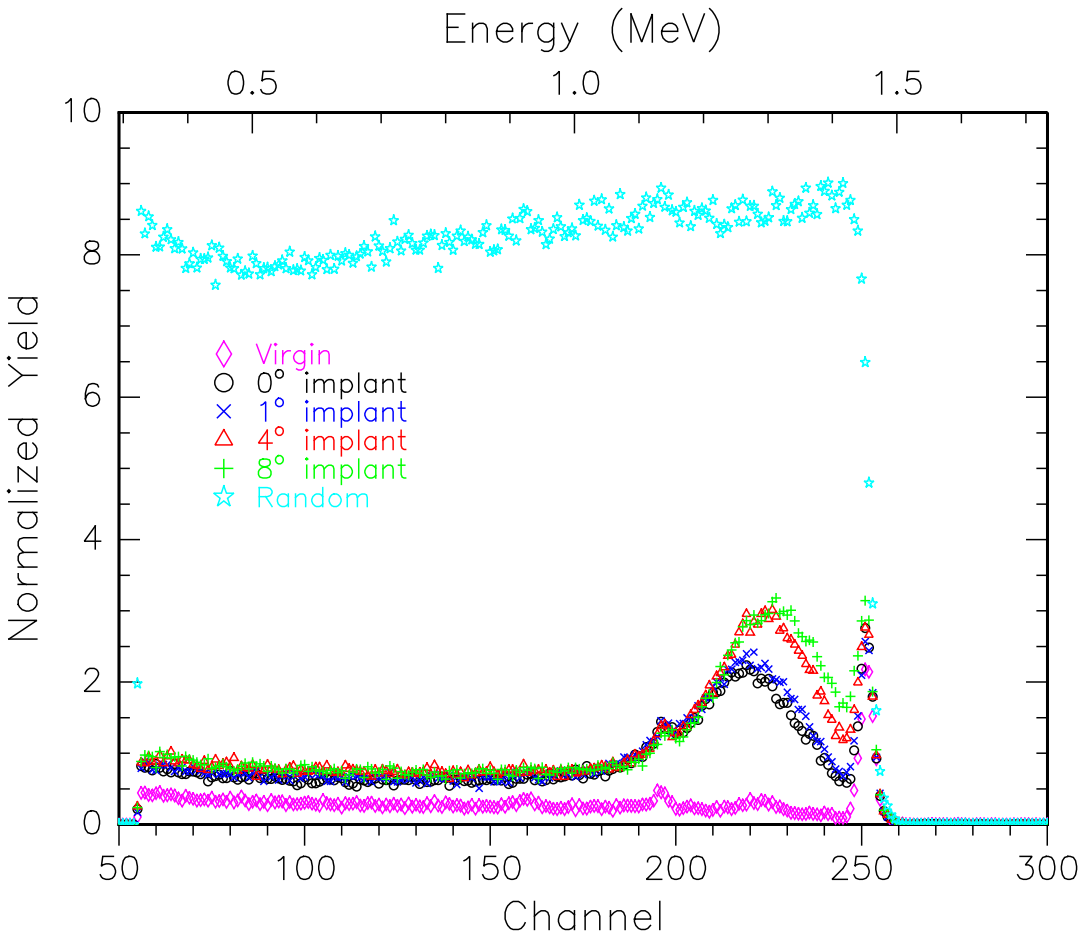

Figure 7.1: RBS-C spectra obtained with 2 MeV He ions 75 keV as-implanted samples.

Chapter 8

Appendix C- DLTS Spectra for Annealed 450 keV Implanted Samples

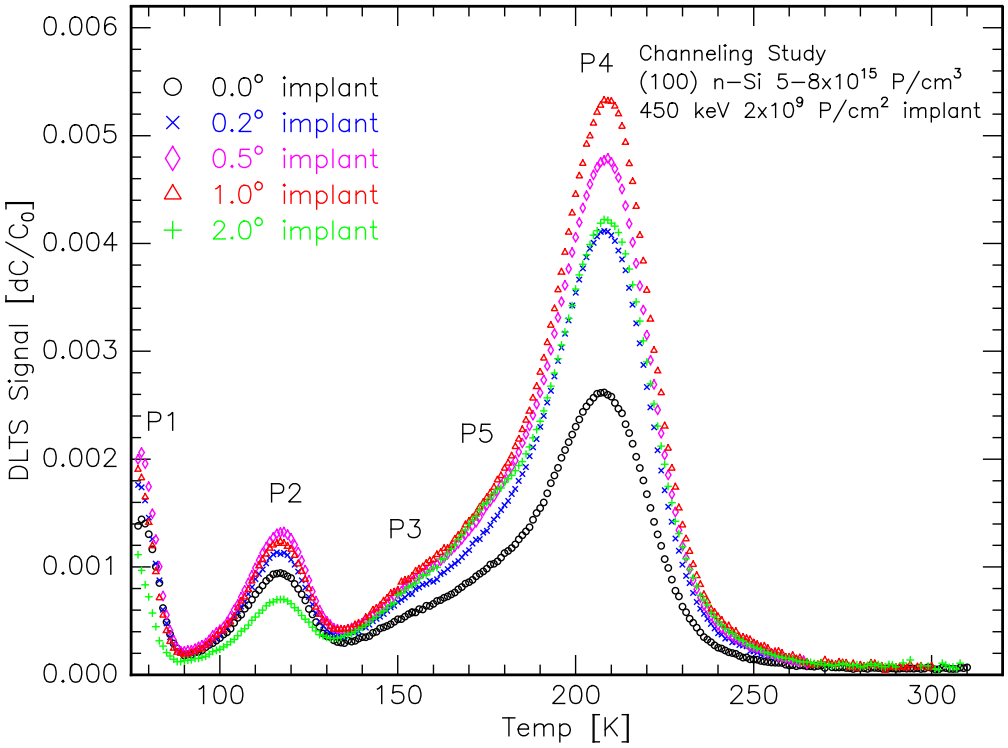

Figure 8.1: DLTS spectra obtained from 80 ms measurement window for 450 keV implanted samples.

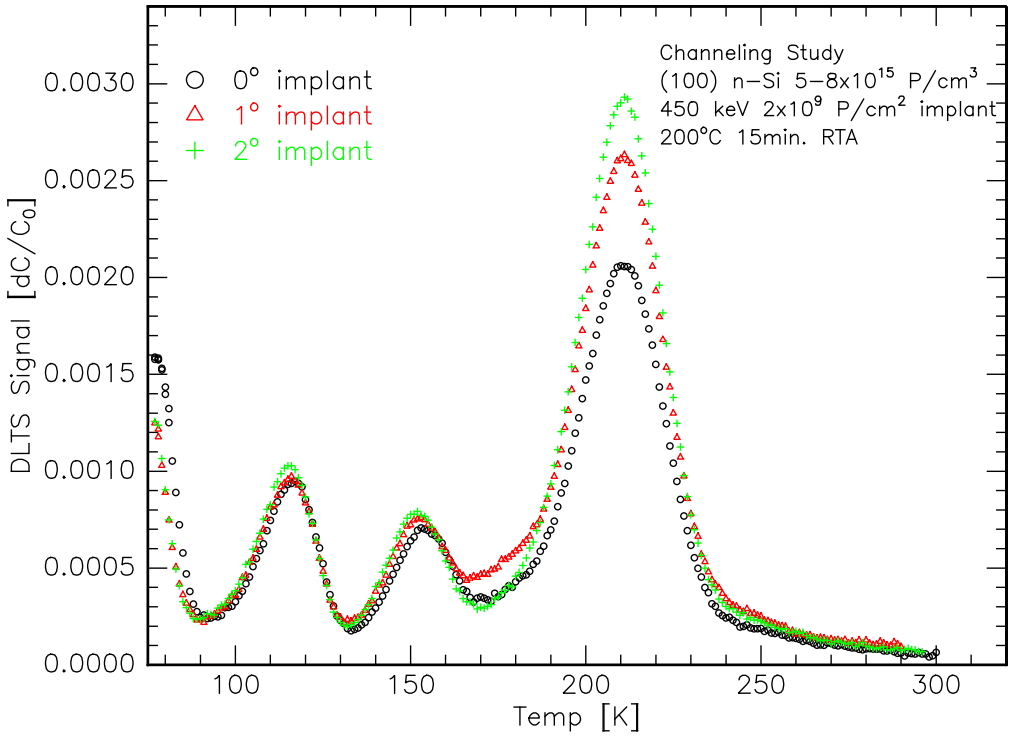

Figure 8.2: DLTS spectra obtained from 80 ms measurement window for 450 implanted samples Rapid Thermal Annealed for 15 min. at 200^{o}C.

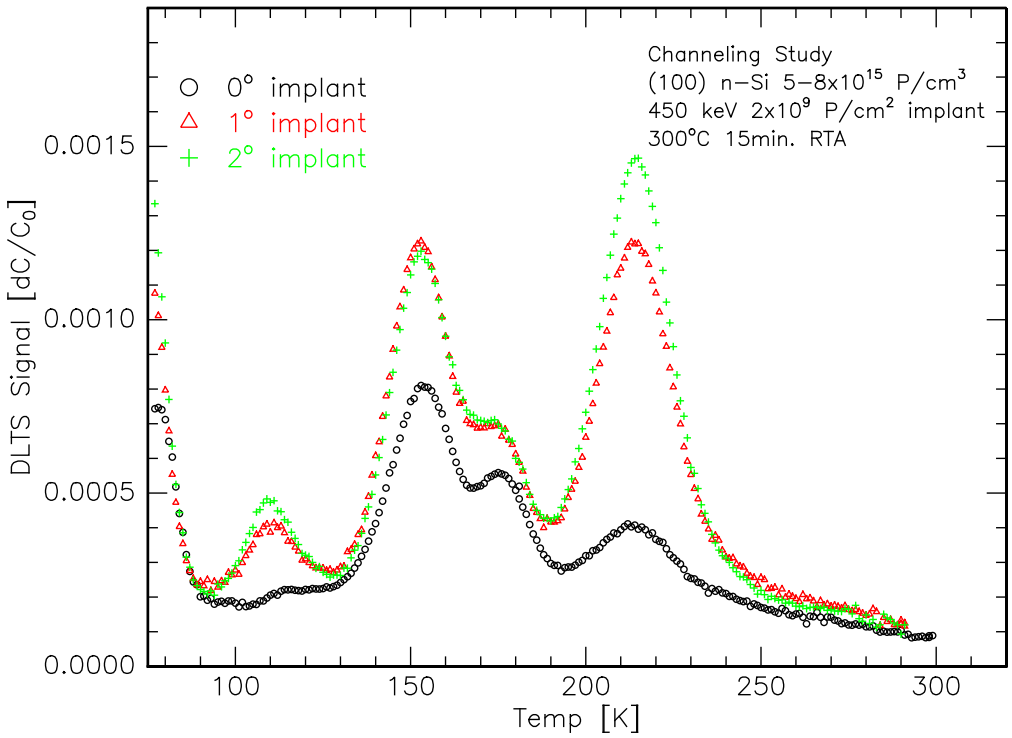

Figure 8.3: DLTS spectra obtained from 80 ms measurement window for 450 implanted samples Rapid Thermal Annealed for 15 min. at 300^{o}C.

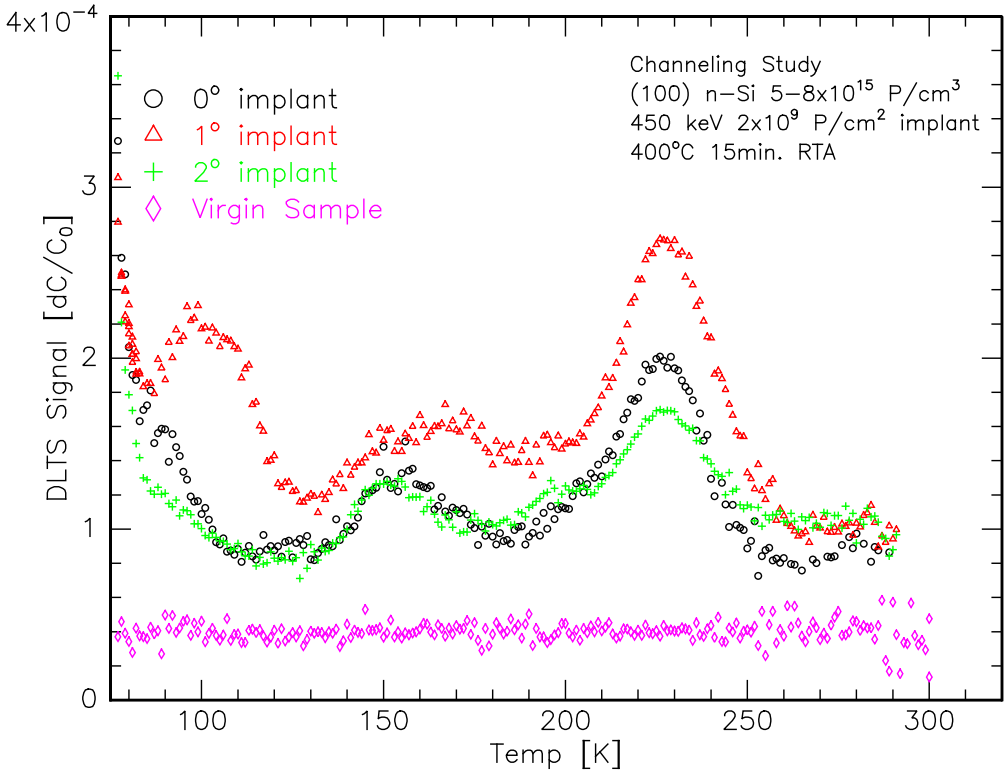

Figure 8.4: DLTS spectra obtained from 80 ms measurement window for 450 implanted samples Rapid Thermal Annealed for 15 min. at 400^{o}C.

Chapter 9

Appendix D- DLTS Defect Depth Profiles for 450 keV Implanted Samples

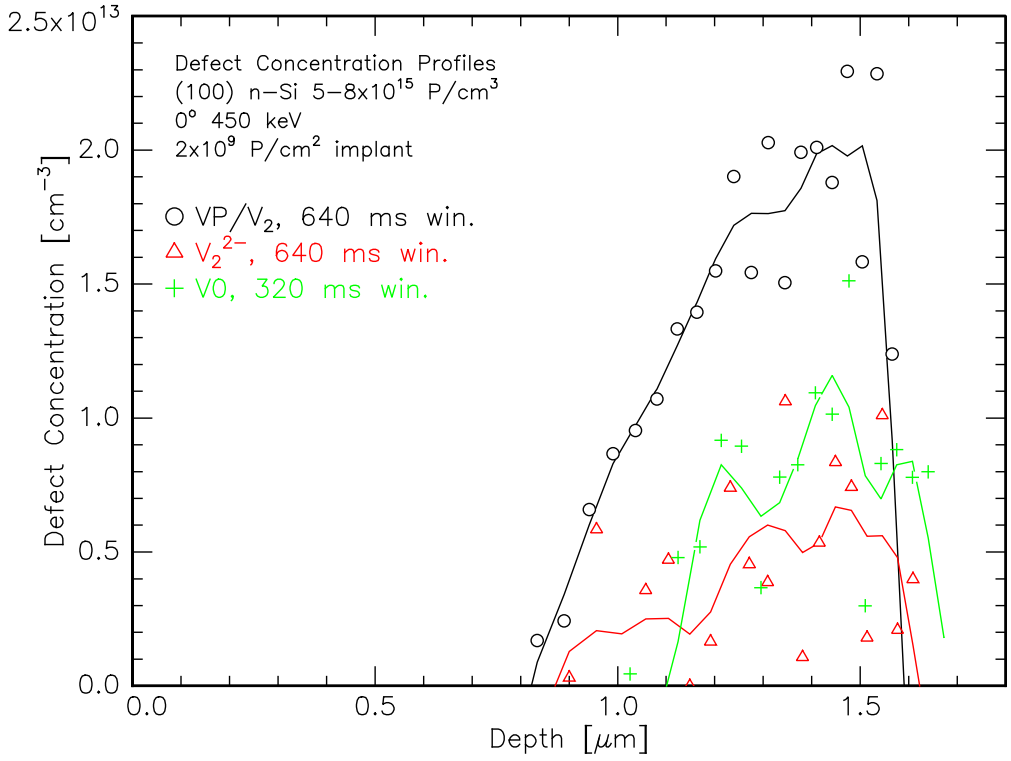

Figure 9.1: Plot of defect depth profiles for sample implanted with 450 keV P at 0^o.

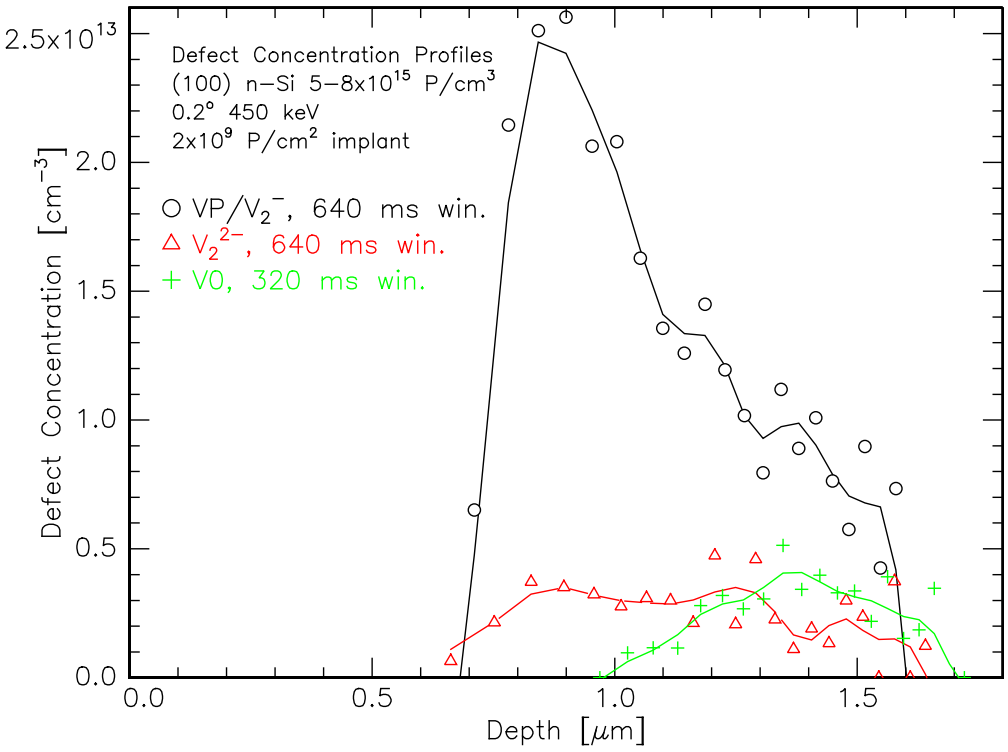

Figure 9.2: Plot of defect depth profiles for sample implanted with 450 keV P at 0.2^o.

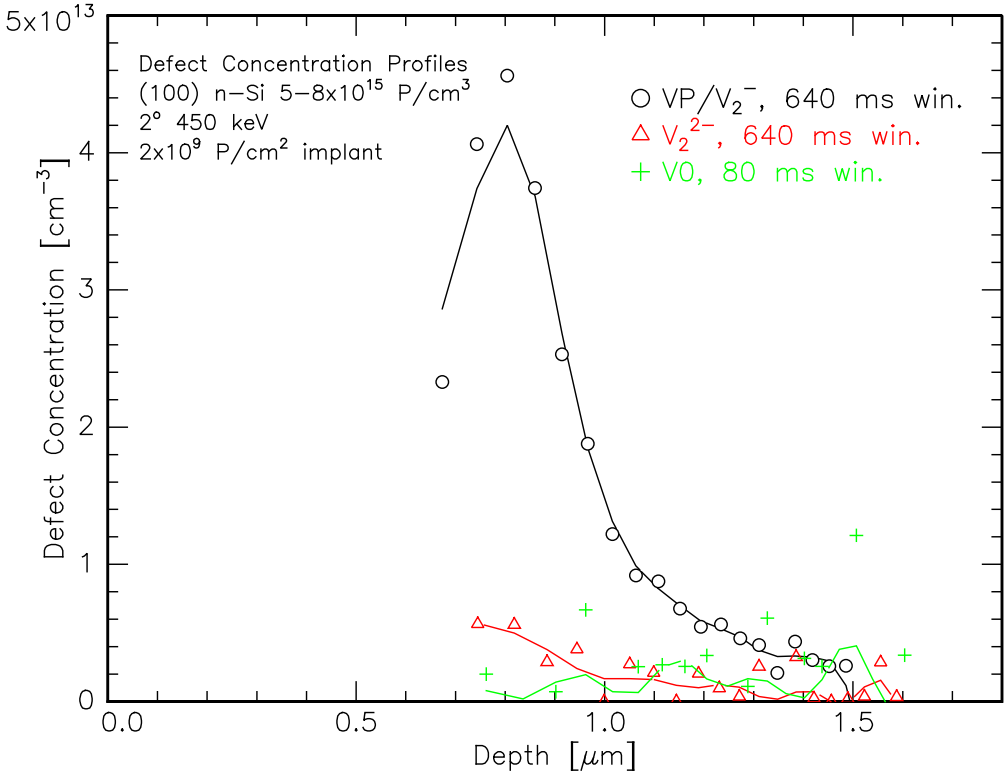

Figure 9.3: Plot of defect depth profiles for sample implanted with 450 keV P at 2^o.

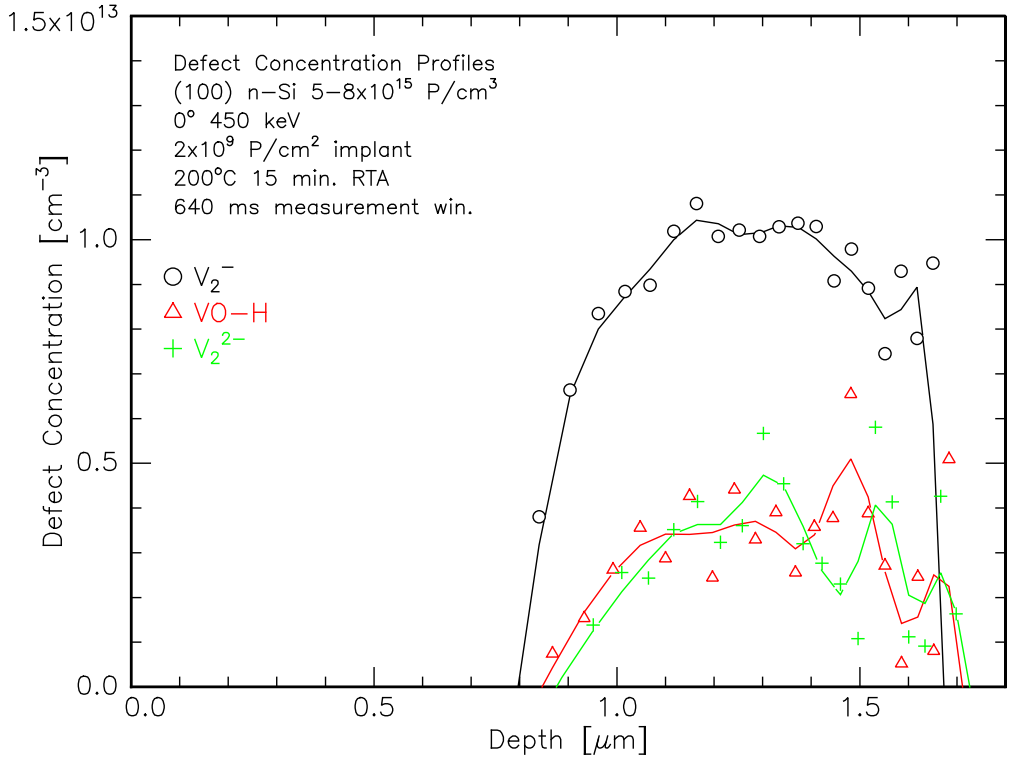

Figure 9.4: Plot of defect depth profiles for sample implanted with 450 keV P at $0^o$and annealed for 15 min.

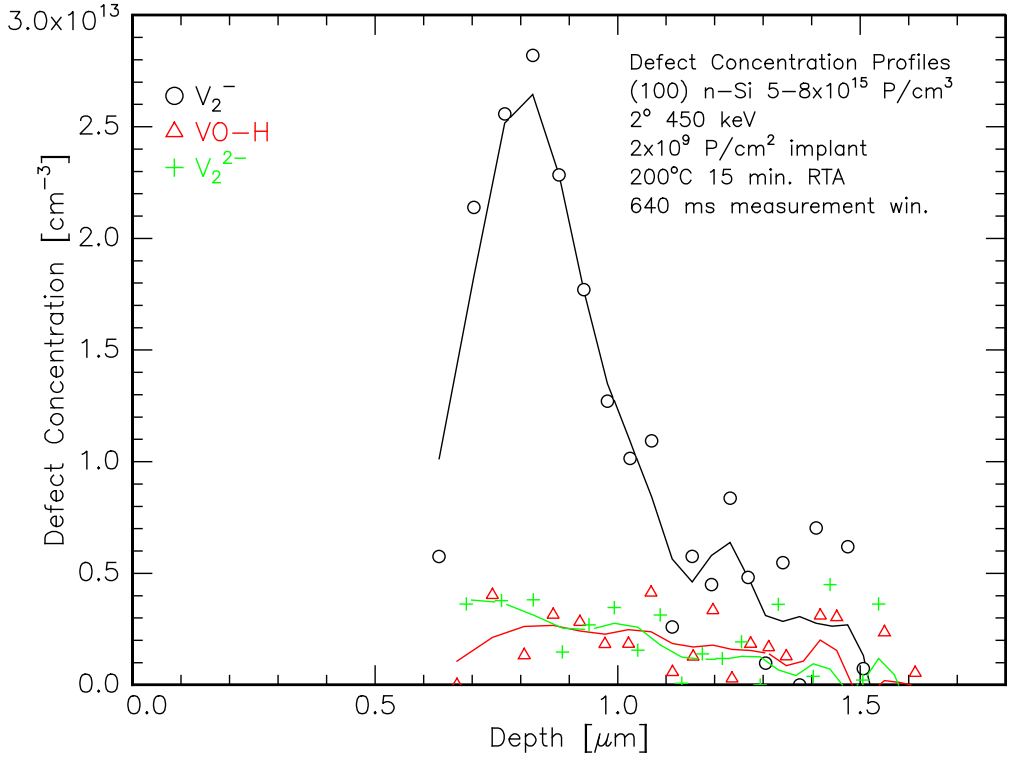

Figure 9.5: Plot of defect depth profiles for sample implanted with 450 keV P at $2^o$and annealed for 15 min.

Bibliography

[1] Wei-Kan Chu, James W. Mayer, and Marc-A. Nicolet. *Backscattering Spectrometry*, pages 223–224. Academic Press, 1978.

[2] Dieter K. Schoder. *Semiconductor Material and Device Characterization.* Wiley Inter–Science.

[3] B. E. Kane. A silicon-based nuclear spin quantum computer. *Nature*, page 133, 1998.

[4] P. N. K. Deenapanray et al. A dlts and rbs analysis of the angular dependence of defects introduced in si during ion beam channeling using 435 kev alpha-particles. *Nclr. Instrmts. and Mthds. in Physcs. Rsrch B*, 136-138:1322–1326, 1998.

[5] B. G. Svensson et al. Divacancy acceptor levels in ion-irradiated silicon. *Phys. Rev. B*, 43(3):2292, 1991.

[6] P. Hazdra et al. The influence of implantation temperature and subsequent annealing on residual implantation defects in silicon. *Nclr. Instrmts. and Mthds. in Physcs. Rsrch B*, 55(1-4):637, 1990.

[7] S. Coffa and F. Priolo. Electrical properties of ion implanted and electron irradiated c-si. In Robert Hull et al., editors, *Properties of Crystalline Si*, page 746. Inspec, EMIS, 1999.

[8] B. G. Svensson et al. Generation of vacancy-type point defects in single collision cascades during swift-ion bombardment of silicon. *Phys. Rev. B*, 55(16):10 498, 1997.

[9] A. Hallen et al. Deep level transient spectroscopy analysis of fast ion tracks in silicon. *J. Appl. Phys.*, 67(3):1266, 1990.

[10] R. J. Schreutelkamp et al. Channeling implantation of b and p in silicon. *Nclr. Instrmts. and Mthds. in Physcs. Rsrch B*, 55:615–619, 1991.

[11] Ning Yu et al. Channeling effect of p implantation in si(100). *Nclr. Instrmts. and Mthds. in Physcs. Rsrch B*, 59:1061–1066, 1991.

[12] V. Raineri et al. Secondary defect reduction by channeling implantation of b and p in (100) silicon. *Nclr. Instrmts. and Mthds. in Physcs. Rsrch B*, 59:1056–1060, 1991.

[13] K. Irmscher et al. Hydrogen–related deep levels in proton–bombarded silicon. *J. Phys. C*, 17:6317, 1984.

[14] Yoichi Kamiura et al. Electronically induced instability of a hydrogen–carbon complec in silicon and its dissociation mechanism. *Jpn J. Appl. Phys.*, 36:6579, 1997.

[15] Yutaka Tokuda et al. Light–illumination–induced transformation of electron traps in hydrogen–implanted n–type silicon. *J. Appl. Phys.*, 86(10):5630, 1999.

[16] Marcel W. Huppi. Proton irradiation of silicon: complete electrical characterization of the induced recombination centers. *J. Appl. Phys.*, 68:2702, 1990.

[17] L. Palmetshofer et al. Defect levels in h^+–,d^+–, and he^+–bombarded silicon. *J. Appl. Phys.*, 72:2167, 1992.

[18] J. Lalita et al. Point defects observed in crystalline silicon implanted by mev si ions at elevated temperatures. *Nclr. Instrmts. and Mthds. in Physcs. Rsrch B*, 96:210, 1995.

[19] S. Livertino et al. Evolution of interstitial– and vacancy–type defects upon thermal annealing in ion–implanted si. *Appl. Phys. Lett.*, 71(3):389, 1997.

[20] Salvatore Coffa and Sebania Libertino. Room–temperature diffusivity of self–intersitials and vacancies in ion–implanted si probed by in situ measurements. *Appl. Phys. Lett.*, 73(23):3369, 1998.

[21] Paolo Pellegrino et al. Impurity–assisted annealing of point defect complexes in ion–implanted silicon. *Physica B*, 273-274:489, 1999.

[22] P. Leveque et al. Hydogen–related defect centers in foat–zone and epitaxial n–type proton implanted silicon. *Nclr. Instrmts. and Mthds. in Physcs. Rsrch B*, 174:297, 2001.

[23] P. Pellegrino et al. Separation of vacancy and interstitial depth profiles in ion-implanted silicon: Experimental observation. *Appl. Phys. Lett.*, 78(22):3442, 2001.

[24] P. Pellegrino et al. Annealing kinetics of vacancy–related defects in low–dose mev self–ion–implanted n–type silicon. *Phys. Rev. B*, 64(195211), 2001.

[25] B. G. Svensson et al. Hydrogen–related electron traps in proton–bombarded float zone silicon. *Mat. Sci. & Eng. B*, 4:285, 1989.

[26] E. H. Rhoderick. *Metal-Semiconductor Contacts*, page 10. Oxford University Press, first edition, 1978.

[27] P. Blood and J. W. Orton. *The Electrical Characterization of Semiconductors: Majority Carriers and Electron States*, page 344. Academic Press, 1992.

[28] E. H. Rhoderick and R. H. Williams. *Metal-Semiconductor Contacts*, page 168. Oxford Science Publications, second edition, 1998.

[29] Oak ridge national laboratory. http://www.ssd.ornl.gov/Programs/MARLOWE/MARLOWE.html.

[30] Leonard C. Feldman and James W. Mayer. *Fundamentals of Surface and Thin film analysis*, page 48. Prentice Hall, 1986.

[31] Leonard C. Feldman, James W. Mayer, and S. Thomas Picraux. *Materials Analysis by Ion Channeling.* Academic Press, 1982.

[32] J. F. Zeigler. *J. Appl. Phys.*, 43(23):2973, 1972.

[33] Michael I. Current et al. Planar channeling effects in si(100). *Nclr. Instrmts. and Mthds. in Physcs. Rsrch B*, 6(23):336, 1985.

[34] James F. Gibbons. Ion implantation in semiconductors–part i range distribution theory and experiments. *Proceedings of the IEEE*, 56(3):295, 1968.

[35] C. Jagadish, B. G. Svennson, et al. Point defects in n-type silicon implanted with low doses of mev boron and silicon ions. *Semiconductor Science and Technology*, 8:481, 1993.

[36] C. Jagadish, B. G. Svennson, et al. Deep level transient spectroscopy study of defects in megaelectronvolt germanium ion implanted silicon. *Thin Solid Films*, 222:173, 1992.